

Contents lists available at ScienceDirect

Journal of the Mechanics and Physics of Solids

journal homepage: www.elsevier.com/locate/jmps





On topology optimization with gradient-enhanced damage: An alternative formulation based on linear physics

Jonathan B. Russ, Glaucio H. Paulino *

Department of Civil and Environmental Engineering, Princeton University, Princeton, NJ 08544, USA Princeton Materials Institute (PMI), Princeton University, Princeton, NJ 08544, USA

ARTICLE INFO

Keywords: Gradient-enhanced damage Topology optimization Local constraints Load capacity

ABSTRACT

Numerous topology optimization formulations have been proposed in order to enhance structural resistance to material failure. A clear line can often be drawn between those methods which attempt to constrain local failure criteria and those that explicitly model the failure physics during the optimization process. In this work the former method is extended in a manner inspired by the mathematical form of typical gradient-enhanced damage models. Importantly, the proposed formulation relies on linear physics during the optimization procedure, which greatly increases its speed and robustness, both of which are essential in industrial applications where large numerical models are typically used. The size effect introduced by using such a numerical model is further investigated and select observations are provided, such as spurious "fin-like" patterns that emerge depending on the type of structure and loading conditions. Finally, the load capacity is verified for each optimized design through a post-optimization verification procedure which is unaffected by the density-based design parameterization and associated material interpolation schemes.

1. Introduction

Since the birth of density-based topology optimization (Bendsøe and Kikuchi, 1988), the method has been continuously studied and improved in a variety of engineering contexts. One important example of this is manifest in structural design optimization in which material failure must often be considered. Although there are many emerging works in this particular area, it is often important to step back and ask seemingly simple questions as these strategies become more complex. Importantly, many approaches involving the direct simulation of failure during an optimization procedure are often inaccessible to those in industry, not only due to the potential lack of access to such design software, but also the immense computational burden of such methods. In particular, this becomes blindingly apparent when confronted with a practical engineering design challenge in which one forward simulation may require hours or days to complete. In this article, we take a different approach and attempt to provide a different formulation and perspective for practical engineering design in the context of material failure as the field continues to progress.

First, it is important to distinguish between at least two types of failure resistance. The first is often related to the peak load capacity of a structure, which is also the focus of this work. The second typically refers to the external energy required, not only to nucleate, but also to *propagate* cracks. The vast majority of existing topology optimization formulations attempt to control crack/damage nucleation (since controlling propagation in this context is ill-conditioned (Baier, 1994)). Many of these approaches indirectly address this problem by imposing constraints on some measure/indicator of material failure. This could be a stress/strain criterion (e.g., Giraldo-Londono and Paulino, 2020), or something like a ductile failure indicator (e.g., Li and Khandelwal, 2017;

^{*} Corresponding author at: Department of Civil and Environmental Engineering, Princeton University, Princeton, NJ 08544, USA E-mail address: gpaulino@princeton.edu (G.H. Paulino).

Russ and Waisman, 2020a). The benefit of such formulations is often the significant reduction in computational expense relative to formulations relying on explicit failure simulation during the optimization process. In this work, we also advocate for such an approach albeit with a different perspective on how to select such a criterion.

In the second case in which nucleation/initiation of damage is explicitly modeled during optimization, the so called "smeared crack" models have been primarily been adopted, largely due to the lack of path tracking and absence of required mesh modification, which greatly simplifies the sensitivity analysis. It is now well-known that local damage models lead to spurious mesh-dependence (Bažant et al., 1984; Pijaudier-Cabot and Bažant, 1987), and that the problem may be regularized by introducing a characteristic material length scale. As Bažant and Jirásek (2002) have previously noted, this length scale in the context of nonlocal continuum damage mechanics should be approximately equal to the width of the fracture process zone (FPZ) of the material and is motivated, at least in part, by the size effect observed in many experiments. Examples of this intrinsic material length scale can be found in Hillerborg et al. (1976) and Gao et al. (1999).

Many topology optimization formulations relying on explicit material failure simulation during the optimization procedure have been proposed in the past decade. James and Waisman (2014) advocated for constraining the damage predicted using a nonlocal continuum damage formulation via a constraint aggregation technique. Prior to this, Amir and Sigmund (2013) employed the "implicit gradient" continuum damage model proposed by Peerlings et al. (1996) in order to optimize the layout of reinforcement in concrete using truss optimization methods. Subsequently, Amir (2013) extended this framework to also incorporate optimization of the concrete structure, in addition to its reinforcement using the same gradient-enhanced continuum damage model. Most recently, Barbier et al. (2022) proposed a method for obtaining minimum weight structures with a user-specified load capacity. In their work, a similar gradient-enhanced damage formulation is used during the optimization process, and a separate linear physics formulation based on an unconverged damage field is proposed to reduce the computational expense relative to the fully nonlinear damage model. While the formulation we propose also relies on linear physics during the optimization procedure, our approach differs in a number of important ways, including a straightforward physical/mathematical interpretation of the optimized/constrained quantities in terms of the considered damage model. This we suggest in addition to the ease with which this formulation could be extended to other similar failure models (e.g., phase-field fracture) and to design problems involving dynamic loading.

While other failure models have been explored in the topology optimization literature (e.g., Xia et al., 2018; Russ and Waisman, 2020b), herein we focus specifically on the gradient-enhanced damage formulation of Peerlings et al. (1996), which was also used in many of the aforementioned topology optimization works. Additionally, we should also note the gradient-enhanced ductile damage topology optimization formulation of Li et al. (2018), based in part on the work of Engelen et al. (2003).

The goal of this work is to provide an alternative efficient/robust topology optimization formulation for designing structures with a specified load capacity. In particular, we target industrial applications in which a particular gradient-enhanced damage model is capable of predicting material failure sufficiently accurately in the context of anticipated loading conditions. The effect of the design domain size relative to the length scale associated with the gradient-enhancement is explored. Importantly, the anticipated range of applicability of this formulation is discussed, including its limitations and side effects that may be encountered in practice.

The remainder of the paper is organized as follows: In Section 2, the density-based design parameterization is introduced, along with the employed filtering and projection schemes. The details of the linear physics formulation used during the optimization process are then outlined in Section 3, followed by the optimization problem statement and analytical sensitivity analysis in Section 4. The complete procedure is described in Section 5, in addition to the post-optimization verification process we use to assess the performance of each design, and many numerical results for two (proposed) benchmark test problems. In Section 6, concluding remarks are offered which summarize our findings, including important observations and limitations of the proposed formulation. For the interested reader, multiple appendices are included for clarity/convenience. Appendix A provides additional details of the damage formulation used during post-optimization load capacity verification. Appendix B briefly clarifies the length scale parameter associated with gradient-enhancement, and Appendix C demonstrates the importance of the gradient-enhanced strain. Appendices D and E address important effects of two parameters in certain design problems. Appendix F provides explicit derivatives of the relevant quantities, completing the analytical sensitivity analysis.

2. Density-based design parameterization

In the optimization formulation, the standard SIMP² (Bendsøe, 1989; Zhou and Rozvany, 1991) design parameterization is used and a single material is considered. Each finite element, e, in the discretized design domain is assigned a scalar pseudo-density, $\rho_e \in [0,1]$, which is used to interpolate certain material properties (e.g., the elastic modulus). A penalization exponent, p, is also introduced in order to drive the pseudo-densities towards a 0/1 (white/black) design. The optimizer controls the design variables, $z \in [0,1]^{N_{elem}}$, which are subsequently filtered, introducing a design length scale, r_{\min} , which alleviates mesh-dependency and other instabilities (Sigmund and Petersson, 1998). In this work, the PDE (Partial Differential Equation) filter with consistent boundary conditions proposed by Wallin et al. (2020) is used in which the PDE and corresponding boundary conditions,

$$-r^2 \nabla \cdot \nabla \hat{\rho} + \hat{\rho} = z \text{ , in } \Omega$$
 (2.1)

¹ Although we focus on the quasi-brittle case for simplicity, the strategy we propose for formulating the optimization problem could be applied considering the ductile damage model used by Li et al. (2018) as well, in a manner similar to Li and Khandelwal (2017) or Russ and Waisman (2020a), albeit via locally constraining the gradient-enhanced equivalent plastic strain.

² SIMP: Solid Isotropic Material with Penalization

$$-r^2\nabla\hat{\rho}\cdot\mathbf{n}=r\hat{\rho}\,\,,\,\,\mathrm{on}\,\,\partial\Omega\setminus(\partial\Omega^u\cup\partial\Omega^t)$$

$$-r^2\nabla\hat{\rho}\cdot\mathbf{n}=0$$
 , on $\partial\Omega^u\cup\partial\Omega^t$ (2.3)

are solved for the filtered field, $\hat{\rho}$, using the same finite element mesh. As shown by Lazarov and Sigmund (2011), the parameter, r, can be related to the classical filter radius, r_{\min} , via the expression, $r = r_{\min}/(2\sqrt{3})$. Note that we have only applied the boundary penalty to the portion of the entire boundary, $\partial \Omega$, that does not correspond to an imposed displacement boundary condition ($\partial \Omega^t$) or an applied traction boundary condition ($\partial \Omega^t$). This distinction is made in order to avoid penalizing the pseudo-densities where the relevant boundary conditions in the physics-based forward analyses are imposed.

Subsequently, the smooth Heaviside projection scheme of Wang et al. (2011) is used, which helps to significantly reduce the amount of intermediate densities which appear in the final design. The filtered field evaluated at the centroid of element e (i.e. $\hat{\rho}_e$) is used to produce the corresponding element density via,

$$\rho_e(\hat{\rho}_e(z)) = \frac{\tanh(\beta_H \eta_H) + \tanh(\beta_H (\hat{\rho}_e - \eta_H))}{\tanh(\beta_H \eta_H) + \tanh(\beta_H (1 - \eta_H))} \tag{2.4}$$

where β_H controls the strength of the projection and η_H controls the value of $\hat{\rho}_e$ where the transition takes place. In all subsequently presented examples η_H is set to 0.5 and continuation is applied to both β_H and p as detailed in Section 5.

3. Linear gradient-enhanced equivalent strain formulation

Here we outline the linear physics formulation used in this work, based on the gradient-enhanced continuum damage formulation of Peerlings et al. (1996). First, we solve the traditional quasi-static linear momentum equation in the absence of body forces based purely on linear elastic mechanics,

$$-\nabla \cdot \boldsymbol{\sigma} = \mathbf{0} \text{ in } \Omega \tag{3.1}$$

$$n \cdot \sigma = t \text{ on } \partial \Omega^t$$
 (3.2)

for a general continuum body, Ω , with boundary $\partial\Omega$. A traction load, t, is applied to $\partial\Omega^t\subset\partial\Omega$ and displacements are imposed on $\partial\Omega^u\subset\partial\Omega$ where $\partial\Omega^t\cap\partial\Omega^u=\emptyset$. Small strain theory is assumed and the corresponding small strain tensor is computed in the standard manner via the relation, $\varepsilon=\operatorname{sym}(\nabla u)$. The Cauchy stress may then be expressed via

$$\sigma = \chi_F(\rho_e) \, \mathbb{C}_0 : \varepsilon(\mathbf{u}), \text{ defining } \chi_F(\rho_e) \equiv \varepsilon + (1 - \varepsilon)\rho_e^p$$
 (3.3)

where $[\mathbb{C}_0]_{ijkl} = \bar{\lambda}\delta_{ij}\delta_{kl} + \mu\left(\delta_{ik}\delta_{jl} + \delta_{il}\delta_{jk}\right)$, $\mu = E_0/[2(1+\nu)]$, and $\bar{\lambda} = E_0\nu/[1-\nu^2]$ in plane stress. The ersatz parameter, ϵ , is included and set to 10^{-9} in all numerical examples presented herein. The parameter E_0 corresponds to the elastic modulus of the solid material, and ν represents Poisson's ratio.

An approximate solution to this boundary value problem is obtained via a standard Galerkin finite element procedure in which the element residual vector may be expressed as

$$R_{u_o} = f_{int}^e - f_{ext}^e \tag{3.4}$$

$$f_{int}^{e} = \sum_{q=1}^{N_{quad}} \left[\mathbf{B}_{u}^{T} \boldsymbol{\sigma}_{e_{q}} \right] w_{e_{q}} \text{, where } \boldsymbol{\sigma}_{e_{q}} = \chi_{E}(\rho_{e}) \ \mathbb{C}_{0} : \boldsymbol{\varepsilon}_{e_{q}}$$

$$(3.5)$$

$$\boldsymbol{f}_{ext}^{e} = \sum_{q=1}^{N_{quad}^{s}} \left[\boldsymbol{N}_{u}^{T} \boldsymbol{t}_{e_{q}} \right] w_{e_{q}}$$
(3.6)

and N_u/B_u contain the values of the shape functions and their derivatives at the appropriate quadrature points.³ The global system of equations, $R_u = f_{int} - f_{ext}$, is then assembled from the element contributions following the usual methodology (i.e., $f_{int} = A_{e=1}^{N_{elem}} f_{int}^e$ and $f_{ext} = A_{e=1}^{N_{elem}} f_{ext}^e$). The solution of $R_u = 0$ for \underline{u} may be obtained in a single Newton iteration according to,

$$\frac{\partial R_u}{\partial u}\Big|_{u=0} \underline{u} = -R_u\Big|_{u=0} \tag{3.7}$$

where $\frac{\partial R_u}{\partial u}$ is the standard linear elastic stiffness matrix.

With the displacement solution, we then wish to compute an approximation of the gradient-enhanced equivalent strain field which ultimately drives the development of damage in the mathematical model briefly described in Appendix A. Namely, we wish to solve,

$$-c\nabla \cdot \nabla \bar{\epsilon} + \bar{\epsilon} = \epsilon_{eg} \text{ in } \Omega \tag{3.8}$$

$$\mathbf{n} \cdot \nabla \bar{\epsilon} = 0 \text{ on } \partial \Omega$$
 (3.9)

³ Note that the shape function derivatives of B_u are evaluated at the N_{quad} volumetric quadrature points, while the shape functions, N_u , shown in Eq. (3.6) have been restricted to the boundary $\partial \Omega^t$ and are evaluated at the corresponding N_{quad}^s surface integration points. The same is true for w_{e_q} in each case which represents the corresponding Jacobian determinant of the isoparametric mapping multiplied by the appropriate quadrature weight.

in which the equivalent strain measure, ε_{eq} , de Vree et al. (1995) is computed according to

$$\varepsilon_{eq}(\varepsilon) = \frac{k-1}{2k(1-2\nu)}I_1 + \frac{1}{2k}\sqrt{\left(\frac{k-1}{1-2\nu}I_1\right)^2 + \frac{12k}{(1+\nu)^2}J_2}$$
(3.10)

where k represents the ratio of compressive-to-tensile strength, $I_1 = \varepsilon_{ii}$, and $J_2 = (1/2)\varepsilon_{ij}^{dev}\varepsilon_{ij}^{dev}$ where $\varepsilon_{ij}^{dev} = \varepsilon_{ij} - (1/3)I_1\delta_{ij}$. The parameter, c, is proportional to $\mathscr{C}_{\bar{\epsilon}}^2$ where $\mathscr{C}_{\bar{\epsilon}}$ is a characteristic length scale for the gradient-enhanced equivalent strain measure. Here we set $c = \mathscr{C}_{\bar{\epsilon}}^2$ per the discussion in Appendix B. Using the nodal displacements, \underline{u} , obtained from solving Eq. (3.7), the equivalent strain measure, ε_{eq} , is then computed. Following a similar finite element procedure with appropriate shape functions and their derivatives (i.e., $N_{\bar{\epsilon}}$ and $B_{\bar{\epsilon}}$) produces the following element level residual equation,

$$\boldsymbol{R}_{\bar{\varepsilon}_{e}} = \sum_{q=1}^{N_{quad}} \left[\left(\chi_{c}(\rho_{e}) \ c \ \boldsymbol{B}_{\bar{\varepsilon}}^{T} \boldsymbol{B}_{\bar{\varepsilon}} + \boldsymbol{N}_{\bar{\varepsilon}}^{T} \boldsymbol{N}_{\bar{\varepsilon}} \right) \underline{\bar{\varepsilon}} - \chi_{\varepsilon_{eq}}(\rho_{e}) \ \boldsymbol{N}_{\bar{\varepsilon}}^{T} \varepsilon_{eq}(\underline{\boldsymbol{u}}) \right] w_{e_{q}}$$

$$(3.11)$$

which is then assembled into its global counterpart, $\mathbf{R}_{\bar{\epsilon}} = \mathcal{A}_{e=1}^{N_{elem}} \mathbf{R}_{\bar{\epsilon}_e}$. Finally, noting that the system $\mathbf{R}_{\bar{\epsilon}} = \mathbf{0}$ is linear in the unknown nodal gradient-enhanced equivalent strains $(\underline{\bar{\epsilon}})$, a single Newton iteration provides the solution via the linear system,

$$\frac{\partial R_{\bar{\varepsilon}}}{\partial \bar{\varepsilon}}\Big|_{\bar{\varepsilon}=0} \bar{\varepsilon} = -R_{\bar{\varepsilon}}\Big|_{\bar{\varepsilon}=0} \tag{3.12}$$

concluding the forward analysis.

Note that both c and ε_{eq} are interpolated using the interpolation functions represented by $\chi_c(\rho_e)$ and $\chi_{\varepsilon_{eq}}(\rho_e)$, respectively, in a similar manner to Li et al. (2018). However, the penalization exponents we take are different for reasons which we now elaborate. First, the authors are not aware of any homogenization-based argument for interpolating a strain measure like the equivalent strain, ε_{eq} . In fact, many arguments in continuum damage mechanics are based on the hypothesis of strain equivalence (Simo and Ju, 1987) in which there is an approximate analogy with the pseudo-density, ρ , if it is viewed as being qualitatively related to an isotropic damage measure, d, via the concept of solid/void volume fractions. However, since the values of the strain measure are often spuriously high in low density regions and these local values can affect neighboring regions via diffusion, we relax this driving force in a manner similar to Bruggi (2008) by setting $\chi_{\varepsilon_{eq}}(\rho_e) = \rho_e^{0.5}$. Taking a smaller magnitude exponent in this case leads to larger values of the gradient-enhanced strain and, therefore, stronger constraints when $\bar{\varepsilon}$ is bounded from above.

Furthermore, in order to prevent the spurious diffusion of the gradient-enhanced strain from regions of high density into regions of low density (artificially lowering the magnitude of \bar{e} in high density regions), the boundary condition expressed in Eq. (3.9) must somehow be enforced internal to the design domain. In an effort to satisfy this requirement and better approximate the physics, the c parameter is interpolated via $\chi_c(\rho_e) = \rho_e$. Taking a penalization exponent greater than 1 increases the difficulty of the optimization problem, however any reasonable positive exponent *should* approximate a no flux condition into a region in which $\rho \approx 0$. Taking larger values results in faster localization (i.e., loss of diffusion) leading to \bar{e} magnitudes that generally increase more rapidly with decreases in ρ . Based on our experience, we set this penalty exponent to 1, which generally achieves a nice balance between enforcing the original no-flux boundary condition internal to the design domain and mitigating some of the additional nonlinearity of the optimization problem which can result from taking larger penalty exponents. Importantly, we elaborate further on this topic in Appendix D and provide an example demonstrating when an alternative choice may be required.

4. Optimization formulation

While there are many existing topology optimization works which consider various strength criteria using linear elastic physics, here we propose an extension with a different strategy/perspective for determining which local quantity to restrict. *If* there exists a known numerical model capable of accurately predicting failure of the selected material under the loading conditions of interest, often the model itself elucidates the useful quantity to constrain. Additionally, many of the mathematical models also make use of a threshold, below which no material degradation occurs.⁴ Furthermore, the relevant local quantity which drives failure is often well-defined with simpler physics (e.g., linear elasticity), resulting in a formulation which is faster numerically and typically more robust for use within a topology optimization framework.

In the gradient-enhanced damage model proposed by Peerlings et al. (1996), the local equivalent strain, ε_{eq} , indirectly drives the evolution of material damage through its gradient-enhanced counterpart, $\bar{\varepsilon}$. However, the damage does not evolve locally until $\bar{\varepsilon}$ exceeds an initial threshold κ_0 , which is a parameter of the model that is calibrated using experimental data. Therefore, locally constraining $\bar{\varepsilon}$ to be less than some fraction of κ_0 when the structure is subject to the design load, may yield structures with the desired load capacity.

Importantly, many of the quasi-brittle materials for which the considered continuum damage formulation was proposed have much higher strength in compression than in tension (e.g., $k \ge 10$). In this case, minimizing the volume of material subject to local

⁴ This is true not only of the gradient-enhanced damage model used for comparison in this work, but is also true of many other numerical methods for failure prediction, notably including the increasingly popular phase-field methods for fracture. For example, see the formulation derived in Miehe et al. (2015) where the tensile strain energy density drives cracking once it exceeds a critical threshold, ψ_c .

⁵ This is also briefly summarized in Appendix A.

constraints on the gradient-enhanced strain results in a behavior similar to constraining only the maximum principal stress (e.g., see Giraldo-Londoño et al., 2022). More specifically, structural regions in compression often become overly thin and the optimization process becomes less stable. To the optimizer, the only apparent utility of keeping compressive members is to transfer loads away from tensile regions, typically by increasing the structure's section modulus. In order to combat this effect, the compliance could be constrained, *however*, an estimate of the compliance corresponding to the lowest weight structure with the desired load capacity is not known *a priori*. Additionally, if the compliance were minimized subject to a constraint on the volume fraction, it would be increasing difficult to know whether the optimization problem is feasible. Therefore, we choose to minimize a weighted sum of the normalized compliance and volume fraction in a manner similar to the formulation proposed by Giraldo-Londoño et al. (2022), with weighting parameter, $\omega \in (0, 1]$. The corresponding mathematical optimization problem is expressed as

$$\min_{\boldsymbol{z} \in [0,1]^{N_{elem}}} \omega \frac{f_{ext}^T \underline{\boldsymbol{u}}}{f_{ext}^T \underline{\boldsymbol{u}}_0} + (1 - \omega) \frac{\rho^T \boldsymbol{V}}{\rho_0^T \boldsymbol{V}}$$
s.t. $\bar{\boldsymbol{\varepsilon}}(\boldsymbol{x}_{e_q}) \leq \bar{\boldsymbol{\varepsilon}}_{max}, \quad e = 1, \dots, N_{elem}, \quad q = 1, \dots, N_{quad}$
with: $\boldsymbol{R}_{\boldsymbol{u}}(\rho, \underline{\boldsymbol{u}}) = \boldsymbol{0}$

$$\boldsymbol{R}_{\bar{\boldsymbol{\varepsilon}}}(\rho, \underline{\boldsymbol{u}}, \underline{\bar{\boldsymbol{\varepsilon}}}) = \boldsymbol{0}$$

$$(4.1)$$

where \mathbf{x}_{e_g} represents the spatial location of the qth quadrature point of element e.⁸ An upper bound, $\bar{\epsilon}_{\max}$, is imposed on the gradient-enhanced equivalent strain measure at each of these quadrature points. In our numerical examples we set $\bar{\epsilon}_{\max}$ to a fraction of the threshold, κ_0 , used in the damage model (i.e., $\bar{\epsilon}_{\max} = \gamma \cdot \kappa_0$, where $\gamma \leq 1$). The compliance and volume fraction are also normalized by their respective values in the first optimization iteration, where the initial nodal displacement vector is represented by $\underline{\boldsymbol{u}}_0$, the initial density vector by ρ_0 , and the vector of element volumes/areas by \boldsymbol{V} .

An Augmented Lagrangian (AL) formulation (Bertsekas, 1999; Nocedal and Wright, 2006) is used to enforce the local constraints in which a solution of Eq. (4.1) is obtained via a sequence of optimization sub-problems. More specifically, at AL step \hat{k} we wish to solve the sub-problem,

$$\min_{\boldsymbol{z} \in [0,1]^{N_{elem}}} \omega \frac{f_{ext}^{T} \underline{\boldsymbol{u}}}{f_{ext}^{T} \underline{\boldsymbol{u}}_{0}} + (1 - \omega) \frac{\rho^{T} \boldsymbol{V}}{\rho_{0}^{T} \boldsymbol{V}} + \frac{1}{N_{elem} \cdot N_{quad}} \sum_{e=1}^{N_{elem}} \sum_{q=1}^{N_{quad}} \left[\hat{\lambda}_{e_{q}}^{(\hat{k})} h_{e_{q}}(\rho_{e}, \underline{\tilde{e}}) + \frac{\hat{\mu}_{e_{q}}^{(\hat{k})}}{2} h_{e_{q}}(\rho_{e}, \underline{\tilde{e}})^{2} \right]$$
with: $R_{\boldsymbol{u}}(\rho, \underline{\boldsymbol{u}}) = \mathbf{0}$

$$R_{\bar{e}}(\rho, \boldsymbol{u}, \bar{e}) = \mathbf{0}$$
(4.2)

where $\hat{\lambda}_{e_q}^{(\hat{k})}$ and $\hat{\mu}_{e_q}^{(\hat{k})}$ represent the Lagrange multiplier estimator and corresponding penalty coefficient for local constraint $h_{e_q}(\rho_e, \bar{\underline{\varepsilon}})$, respectively. The local constraints are defined such that,

$$h_{e_q}(\rho_e, \underline{\bar{e}}) = \max \left(g_{e_q}(\rho_e, \underline{\bar{e}}), -\frac{\hat{\lambda}_{e_q}^{(\bar{k})}}{\hat{\mu}_{e_q}^{(\bar{k})}} \right)$$

$$(4.3)$$

in which the local inequality constraints are expressed piece-wise according to,

$$g_{e_q}(\rho_e, \bar{\underline{e}}) = \begin{cases} \rho_e \left(\frac{N_{\bar{e}}\bar{\underline{e}}}{\bar{e}_{\max}} - 1\right)^2 & \text{, if } N_{\bar{e}}\bar{\underline{e}} \ge \bar{e}_{\max} \\ 0 & \text{, otherwise} \end{cases}$$
(4.4)

consistent with Senhora et al. (2020). After each AL step \hat{k} , the Lagrange multiplier estimators and penalty coefficients are updated via the expressions,

$$\hat{\lambda}_{e_a}^{(\hat{k}+1)} = \hat{\lambda}_{e_a}^{(\hat{k})} + \hat{\mu}_{e_a}^{(\hat{k})} h_{e_a}(\rho_e, \bar{\underline{\epsilon}}) \tag{4.5}$$

$$\hat{\mu}_{e_q}^{(\hat{k}+1)} = \begin{cases} \min\left(\hat{\alpha}\hat{\mu}_{e_q}^{(\hat{k})}, \hat{\mu}_{\max}\right) & \text{, if } h_{e_q}(\rho_e, \underline{\epsilon}) > 0\\ \hat{\mu}_{e_q}^{(\hat{k})} & \text{, otherwise} \end{cases}$$

$$\tag{4.6}$$

where $\hat{\alpha} > 1$ represents the penalty factor update coefficient and $\hat{\mu}_{max}$ is the corresponding upper bound placed on the penalty parameter in order to prevent ill-conditioning.

⁶ In this case, the designer must provide a large enough upper bound on the volume fraction in order to satisfy the local constraints. While this formulation could also potentially work, it would require additional unnecessary guesswork.

⁷ Note that setting $\omega = 1$ (corresponding to no volume fraction consideration) may also be useful in some situations since the load capacity of a fully dense structure may be improved by removing material.

⁸ Typically only a single constraint is needed at the centroid of each element when the constitutive response is path-independent prior to damage initiation. However, we keep the formulation general to easily extend to path-dependent material responses (e.g., elastoplasticity) prior to the onset of damage.

⁹ Consistent with Giraldo-Londono and Paulino (2020) we do not obtain a fully converged solution to each sub-problem, but rather perform $N_{\text{MMA}} = 5$ iterations with the MMA optimizer prior to updating the Lagrange multiplier estimators and penalty coefficients.

 $[\]frac{10}{N}$ Note that we have also introduced the $\frac{1}{N}$ normalization (corresponding to N local constraints) proposed by Senhora et al. (2020).

4.1. Sensitivity analysis

The local constraints portion of the AL objective may be written as a scalar function,

$$f(\boldsymbol{\rho}, \underline{\boldsymbol{u}}, \underline{\bar{\boldsymbol{e}}}) = \sum_{e=1}^{N_{elem}} \sum_{q=1}^{N_{quad}} \left[\hat{\lambda}_{e_q}^{(\hat{k})} h_{e_q}(\boldsymbol{\rho}_e, \underline{\bar{\boldsymbol{e}}}) + \frac{\hat{\mu}_{e_q}^{(\hat{k})}}{2} h_{e_q}(\boldsymbol{\rho}_e, \underline{\bar{\boldsymbol{e}}})^2 \right]$$

$$(4.7)$$

for which we compute the analytical sensitivity. Augmenting this function with the inner product of the unknown vectors λ and μ with the appropriate residual equations,

$$\hat{f}(\rho, \underline{u}, \underline{\bar{\epsilon}}) = f(\rho, \underline{u}, \underline{\bar{\epsilon}}) + \lambda^T R_u(\rho, \underline{u}) + \mu^T R_{\bar{\epsilon}}(\rho, \underline{u}, \underline{\bar{\epsilon}})$$
(4.8)

and taking the derivative of this augmented function with respect to a single pseudo-density, ρ_e , we obtain,

$$\frac{d\hat{f}}{d\rho_{e}} = \frac{\partial f}{\partial\rho_{e}} + \lambda^{T} \frac{\partial \mathbf{R}_{u}}{\partial\rho_{e}} + \mu^{T} \frac{\partial \mathbf{R}_{\bar{\varepsilon}}}{\partial\rho_{e}} + \left(\frac{\partial f}{\partial u} + \lambda^{T} \frac{\partial \mathbf{R}_{u}}{\partial u} + \mu^{T} \frac{\partial \mathbf{R}_{\bar{\varepsilon}}}{\partial u}\right) \frac{d\underline{u}}{d\rho_{e}} + \left(\frac{\partial f}{\partial \bar{\varepsilon}} + \mu^{T} \frac{\partial \mathbf{R}_{\bar{\varepsilon}}}{\partial \bar{\varepsilon}}\right) \frac{d\bar{\underline{\varepsilon}}}{d\rho_{e}}.$$
(4.9)

Here we see that upon choosing λ and μ to satisfy,

$$\frac{\partial \mathbf{R}_{\bar{\varepsilon}}^T}{\partial \bar{\varepsilon}} \mu = -\frac{\partial f}{\partial \bar{\varepsilon}}^T \tag{4.10}$$

$$\frac{\partial \mathbf{R}_{u}}{\partial \underline{u}}^{T} \lambda = -\frac{\partial f}{\partial \underline{u}}^{T} - \frac{\partial \mathbf{R}_{\tilde{\epsilon}}}{\partial \underline{u}}^{T} \mu \tag{4.11}$$

the sensitivity simplifies to fast element level operations corresponding to

$$\frac{d\hat{f}}{d\rho_e} = \frac{\partial f}{\partial \rho_e} + \lambda^T \frac{\partial \mathbf{R}_u}{\partial \rho_e} + \mu^T \frac{\partial \mathbf{R}_{\bar{e}}}{\partial \rho_e}. \tag{4.12}$$

After this derivative is computed for each element, the final required derivative with respect to the design variables, z, is obtained via the chain rule consistent with the filtering and projection operations outlined in Section 2. The required explicit derivatives are provided in Appendix F along with a numerical verification analysis of this analytical calculation.

5. Procedure & numerical results

In addition to demonstrating the potential of the proposed formulation, we also wish to highlight the size effect (i.e., design domain size, L, relative to the gradient-enhancement length scale, $\ell_{\bar{e}}$) and briefly illuminate the effect of the upper bound, $\bar{\epsilon}_{\max}$. In an effort to achieve this, the two test problems illustrated in Figs. 1 and 2 are employed, each parameterized by the scale, L. For each example, three choices of L are explored with identical constitutive parameters, including $\ell_{\bar{e}}$. An identical finite element mesh is used in each case with only isotropic scaling of the nodal coordinates, in addition to consistent scaling of the filter radius, r_{\min} .

In order to study the effect of $\ell_{\tilde{\ell}}$ on an optimized design, the most obvious strategy might correspond to performing the same numerical example with different $\ell_{\tilde{\ell}}$ values. However, this parameter is well-known to greatly affect the physics of the problem and has a large impact on the predicted load capacity. Peerlings et al. (1996) note that this parameter "implicitly introduces an internal length in the constitutive model" and, later, Peerlings et al. (1998) also argue that this length scale must be related to a "characteristic microstructural scale". Therefore, changing this parameter is in some way analogous to changing the elastic modulus, and could therefore be viewed as a parameter corresponding to a different material. Consequently, we do not change the value of $\ell_{\tilde{\ell}}$, but rather change the size of the design domain via the parameter, L. As is elegantly explained by Bažant (2004), if the domain size is large relative to the size of fracture process zone, a quasi-brittle material will behave in a manner more consistent with perfectly brittle theory (i.e. Linear Elastic Fracture Mechanics, LEFM). However, smaller domain sizes relative to the fracture process zone result in increasingly quasi-brittle behavior.

The three domain sizes we examine correspond to $L=L_0=200$ mm, $L=L_0/2=100$ mm, and $L=L_0/4=50$ mm. Additionally, a 1 mm thickness is assumed throughout. In the case of the L-bracket, the finite element mesh consists of 102,400 quadrilateral elements and 103,201 nodes, corresponding to 309,603 degrees of freedom. Similarly, the portal frame finite element mesh consists of 116,595 quadrilateral elements and 117,317 nodes, corresponding to 351,951 degrees of freedom. These domains are illustrated in Figs. 3 and 4, respectively, along with a damage field obtained with $\rho=1$ everywhere (i.e., fully dense). In a further effort to produce design problems which are both challenging and similar at the three domain scales, the magnitude of each design load corresponds to the peak load capacity of the respective fully dense design domain. Table 1 provides the design loads for each example and domain scale, L. A continuation scheme is adopted on both the SIMP exponent, p, and the projection parameter, p. In all numerical examples presented herein, p is set to 1.0 for the first 50 iterations p is subsequently additively increased by 0.5 every 25 optimization iterations until it reaches a maximum value of 3.0. The parameter, p, also begins at 1.0, however we delay its additive update until optimization iteration 150 in order to avoid excessive nonlinearity early in the optimization process. It is then increased by 1.0 every 25 optimization iterations up to a maximum value of 8.0, which is less than the bound, p in p in p is p in p

¹¹ Note that the number of iterations refers to the number of optimizer updates rather than the number of outer AL iterations.

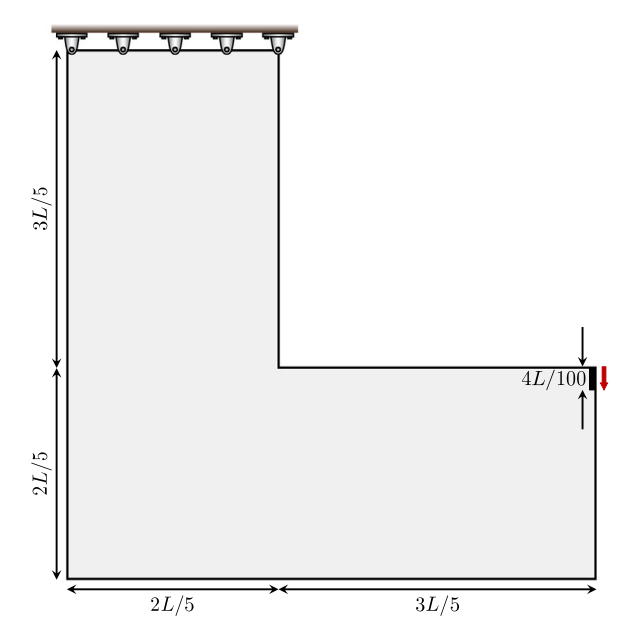


Fig. 1. L-bracket design domain and boundary conditions. Note the passive (i.e. ρ fixed to 1) region shown in black where the downward load is applied.

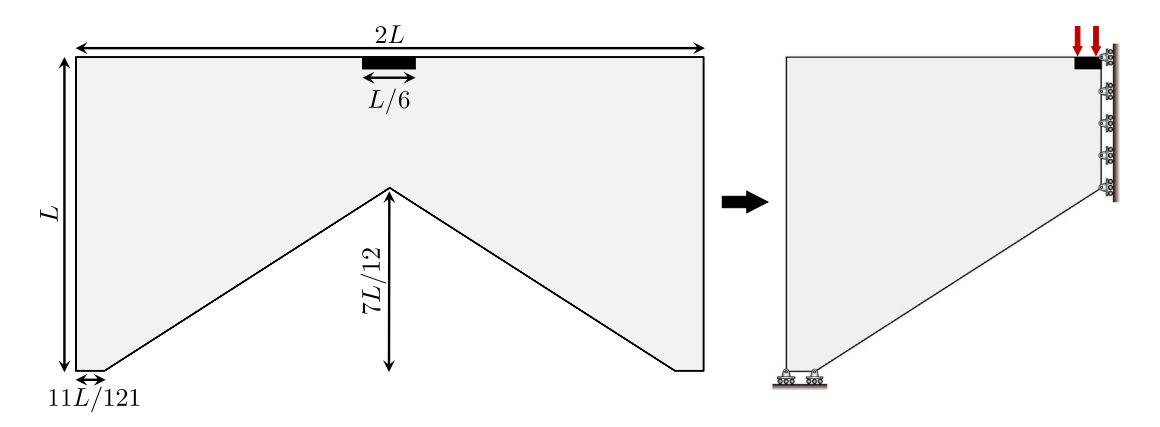


Fig. 2. Portal frame design domain and boundary conditions, including imposed symmetry about the center plane. Note the passive (i.e. ρ fixed to 1) region shown in black where the downward load is applied.

Table 1
Design loads corresponding to the predicted peak load capacity of each fully dense design domain.

L-bracket			Portal frame				
L = 200 mm	L = 200 mm $L = 100 mm$ $L = 50 m$		L = 200 mm $L = 100 mm$ $L = 100 mm$				
18.75 N	11.0 N	6.45 N	23.9 N	14.4 N	8.8 N		

for all presented examples. ¹² The parameters provided in Table 2 are also identical for all numerical examples, and those additionally required during post-optimization verification are provided in Table 3. Note that the constitutive parameters correspond to those provided by Peerlings et al. (1998) for lightweight concrete.

Results for two different upper bounds on $\bar{\epsilon}$ (i.e., $\bar{\epsilon}_{\max} = \kappa_0$ and $\bar{\epsilon}_{\max} = 0.95 \times \kappa_0$) are provided to demonstrate its effect. Furthermore, in each case we desire a set of results corresponding to different values of the weighting parameter, ω . However, as discussed in Section 4, smaller values of ω may lead to numerical instability, particularly when materials with larger ratios of compressive-to-tensile strength (i.e., k) are encountered, which is the case for the material considered in this work (Peerlings et al., 1998 set k to 10). Therefore, we utilize a particularly effective and efficient means of circumventing this issue. Initially, the

 $^{^{12}}$ Refer to da Silva et al. (2021) and note that h_e corresponds to maximum side length of a finite element in the design domain.

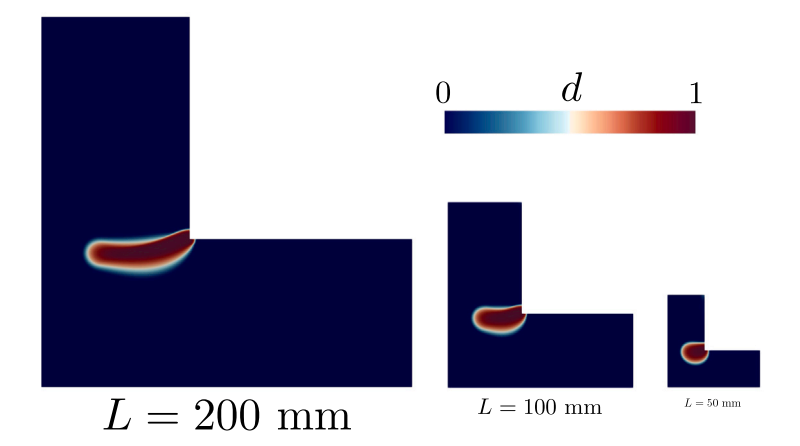


Fig. 3. The damage field for each of three L-bracket examples in which the domain has been scaled by 1, 1/2, and 1/4, respectively. The domains are fully dense (i.e. $\rho = 1$) and 50% additional displacement load is applied beyond the displacement corresponding to the peak load capacity in each case.

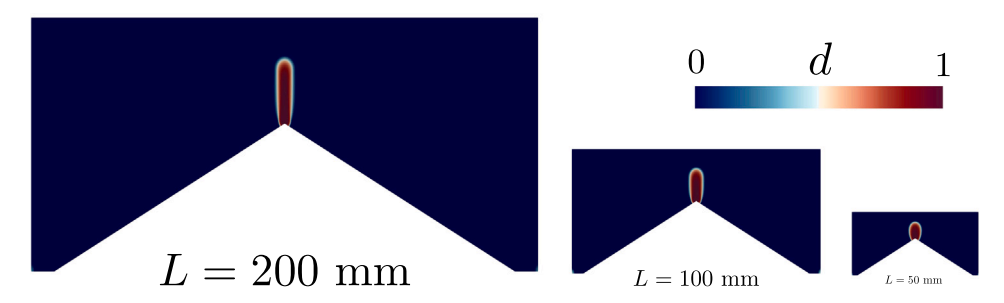


Fig. 4. The damage field for each of three portal frame examples in which the domain has been scaled by 1, 1/2, and 1/4, respectively. The domains are fully dense (i.e. $\rho = 1$) and 50% additional displacement load is applied beyond the displacement corresponding to the peak load capacity in each case.

design variables z and ω are all set to 0.5 and we obtain a converged result after 600 total iterations. ¹³ Subsequently, ω is reduced by 0.1 and 200 additional iterations are performed. This process of reducing ω by 0.1 every 200 additional iterations until we reach a final value of $\omega=0.1$, produces a set of 5 design candidates (corresponding to $\omega\in\{0.5,0.4,0.3,0.2,0.1\}$) with a range of trade-offs between mass and stiffness. ^{14,15} Importantly, we do not evaluate the peak load capacity of each optimized design with the density-based geometry since the mechanical response may be quite different from that obtained using a more traditional CAD representation of the structure and a forward solution without interpolations of the material parameters. In an effort to provide a fair comparison, each optimized topology is extracted to an STL file along the $\rho=0.5$ level set, which approximately preserves the area/volume of the optimized structure. A conforming unstructured quadrilateral mesh is then generated for each STL representation, and the fully nonlinear damage model detailed in Appendix A is used to estimate the peak load capacity. This process is briefly depicted in Fig. 5. Note that since this procedure is decoupled from the optimization process, then higher fidelity physics could ultimately be used to evaluate the optimized designs in a manner similar to Russ and Waisman (2020a), where large deformation kinematics and ductile failure were explicitly modeled after design optimization with lower fidelity physics. Buckling, for example, could therefore be considered in the optimization process only when the post-optimization verification simulations indicate that the structural response is indeed limited by buckling.

 $^{^{13}}$ Here we do not refer to the number of AL iterations, but rather the total number of iterations in the optimizer.

¹⁴ Changing ω during the optimization process is generally much gentler than changing a bound on a constraint directly enforced by the optimizer. The latter may produce a strong drive towards the feasible set and result in unstable behavior.

¹⁵ The optimization problem defined in Eq. (4.2) is solved using a C++ implementation of the Method of Moving Asymptotes (MMA) (Svanberg, 1987, 2007), in which the open source interior point optimizer, IPOPT (Wächter and Biegler, 2006), is used to efficiently solve each optimization subproblem. The forward analyses and sensitivity calculations are performed using an in-house developed C++ code built upon the deal.II (Arndt et al., 2021) finite element library, using PETSc (Balay et al., 2018) for massively parallel linear algebra. Through PETSc, the MUMPS (Amestoy et al., 2001) sparse direct linear solver is used to solve the global linear systems.

¹⁶ This procedure is employed with the hope of obtaining a more accurate prediction of structural load capacity in lieu of more appropriate experimental testing. In this work we take for granted the fact that fracture mechanics is still an open problem for many materials and loading scenarios. As is mentioned in the afterthought of Nguyen et al. (2020), fracture mechanics "has been researched for a century, and probably will be for another century".

Table 2Parameters used during the optimization procedure.

Solid elastic modulus, E_0	18 GPa
Poisson's ratio, v,	0.2
Compression-to-tension strength ratio, k	10
Gradient-enhancement parameter, $c = \ell_{\tilde{\epsilon}}^2$	1.0 mm ²
Initial Lagrange multiplier estimators, $\hat{\lambda}_e^{(1)}$	0
Initial penalty factors, $\hat{\mu}_{e_a}^{(1)}$	10^{2}
Maximum penalty factor, $\hat{\mu}_{max}$	10^{4}
Penalty factor update parameter, $\hat{\alpha}$	1.1
MMA move limit, move	0.05

 Table 3

 Additional parameters used during post-optimization verification

01	
Damage evolution threshold, κ_0	2.1e-4
Damage evolution parameter, α	0.96
Damage evolution parameter, β	350.0
Damage evolution viscosity, η	10^{-4} s

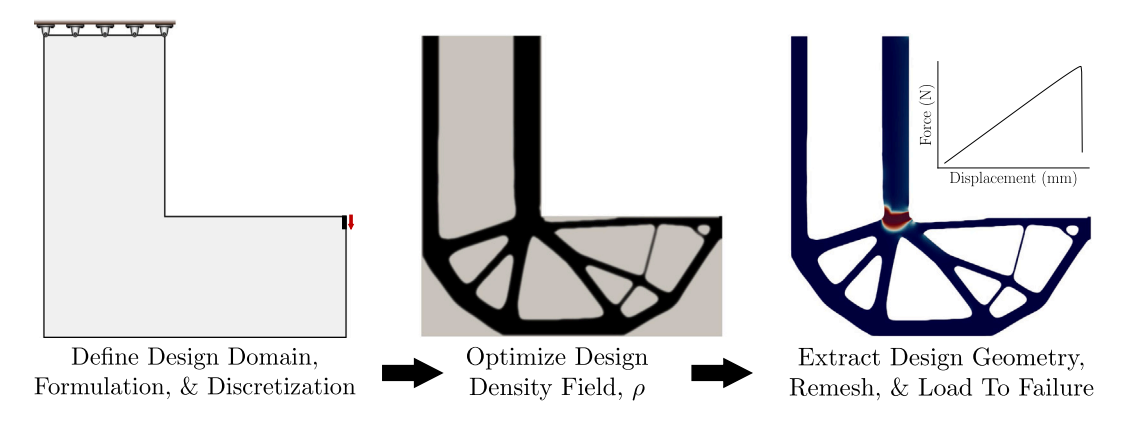


Fig. 5. Post-optimization verification procedure: (1) extraction of the optimized topology to an STL file, (2) conformal remeshing of the extracted geometry, and (3) subsequent forward analysis conducted without density-based interpolation of material properties, using the gradient-enhanced damage model outlined in Appendix A. In this way, the peak load capacity and other important properties may be more accurately estimated in lieu of experiments.

5.1. L-bracket example

Although the L-bracket domain has saturated the majority of the topology optimization literature and many researchers have grown understandably disenchanted with its presentation, it continues to serve as a seemingly simple example, characterized by the ease with which it often highlights the shortcomings of many formulations. More importantly, it frequently furnishes insights when our intuitions are initially violated, and this work is certainly no exception as we shall show. The filter radii for the three design domains are consistently scaled with L, resulting in r_{\min} values of 4 mm, 2 mm, and 1 mm. The results corresponding to $\bar{\epsilon}_{\max} = \kappa_0$ are provided first, with optimized topologies shown in Fig. 6 and corresponding damage field predictions in Fig. 7.¹⁷ The relevant properties predicted post-optimization in each case are provided in Table 4, including the peak load capacity, volume fraction, and the end displacement at 90% of the design load. Additionally, the results corresponding to the tighter upper bound on the gradient-enhanced strain measure (i.e., $\bar{\epsilon}_{\max} = 0.95 \times \kappa_0$) are provided in Figs. 8, 9, and Table 5. All force vs. displacement curves are collected into Fig. 10, in which the design load level is also clearly illustrated for each domain size, L.

A plethora of interesting phenomena are manifest in the results. First, Fig. 10 illustrates the ability of the formulation to produce a variety of designs that meet the load capacity requirement when the domain size is sufficiently large with respect to $\ell_{\tilde{\epsilon}}$ (i.e., L=100 mm and L=200 mm). It also demonstrates that decreasing the upper bound on the gradient-enhanced strain ($\tilde{\epsilon}_{max}$) produces structures with higher load capacity, consistent with our intuition.

However, when the design domain is smaller compared to $\ell_{\tilde{\epsilon}}$ (e.g., L=50 mm), there appears to be more difficulty in achieving the design load capacity. Examining the damage fields illustrated in Figs. 7 and 9 indirectly suggests one potential explanation.

 $^{^{17}}$ Each set of five designs obtained for each domain size (L) required ≈ 3.8 hours running on 4 MPI ranks of a workstation consisting of an Intel Xeon® Gold 6258R CPU and 192 GB of RAM. The corresponding nonlinear damage simulations each required less than 19 min to execute.

¹⁸ Since some designs fail at load levels below the design load capacity, the end displacement corresponding to 90% of the design load provides a consistent, intuitive measure of the structural stiffness in lieu of the compliance.

Table 4 L-bracket post-optimization verification results obtained for $\bar{\epsilon}_{\max} = \kappa_0$. The volume fraction (VF), peak load capacity (PL), and the end displacement (U) are reported. Note that U corresponds to the end displacement at 90% of the design load for each domain size (L).

ω	L = 200 mm			L = 100 r	nm		L = 50 mm		
	VF	PL [N]	U [mm]	VF	PL [N]	U [mm]	VF	PL [N]	U [mm]
0.5	0.407	18.799	0.194	0.423	11.029	0.113	0.443	6.536	0.067
0.4	0.355	18.786	0.218	0.371	11.041	0.128	0.392	6.046	0.076
0.3	0.316	18.840	0.246	0.332	11.037	0.144	0.354	6.065	0.085
0.2	0.288	18.846	0.277	0.303	11.018	0.163	0.324	5.961	0.097
0.1	0.265	18.769	0.325	0.276	10.958	0.196	0.296	5.997	0.117

Table 5 L-bracket post-optimization verification results obtained for $\bar{\epsilon}_{\max} = 0.95 \times \kappa_0$. The volume fraction (VF), peak load capacity (PL), and the end displacement (U) are reported. Note that U corresponds to the end displacement at 90% of the design load for each domain size (L).

ω	L = 200 mm			L = 100 r	nm		L = 50 mm		
	VF	PL [N]	U [mm]	VF	PL [N]	U [mm]	VF	PL [N]	U [mm]
0.5	0.414	19.629	0.193	0.431	11.567	0.114	0.455	6.663	0.069
0.4	0.364	19.663	0.217	0.383	11.587	0.127	0.407	6.353	0.077
0.3	0.326	19.685	0.243	0.347	11.571	0.142	0.373	6.205	0.085
0.2	0.298	19.636	0.274	0.317	11.546	0.162	0.343	6.196	0.096
0.1	0.276	19.556	0.322	0.287	11.395	0.197	0.318	6.127	0.115

Nearly, all optimized structures corresponding to L=200 mm and L=100 mm fail in a region near the re-entrant corner, however, optimized designs corresponding to L=50 mm mostly fail elsewhere in structural members which are thin relative to $\ell_{\bar{e}}$. Although we employ the projection scheme in Eq. (2.4), a transition region of intermediate densities with finite thickness inevitably remains. In this region, the interpolation of the parameter c (i.e., $\chi_c(\rho_e)$) can have a large impact on the resulting approximation of the no-flux boundary condition in Eq. (3.9). Larger member sizes, typically corresponding to larger domains, are relatively unaffected by this issue of allowing too much diffusion into low density regions, and in these cases the standard $\chi_c(\rho_e) = \rho_e$ appears to be sufficient. However, as we show in Appendix D, it is necessary to increase the penalization exponent in $\chi_c(\rho_e)$ when the structural member cross-section is approximately less than $2\ell_{\bar{e}}$, which is often the case for smaller design domains. The result is better enforcement of the no flux boundary condition internal to the design domain, highlighting that special care must be taken when selecting an interpolation function penalty exponent for the parameter c.

Perhaps unsurprisingly, yet another interesting observation arises when L is small relative to $\ell_{\bar{\epsilon}}$ (i.e., $L/\ell_{\bar{\epsilon}}$ approximately less than 100). While also present in Fig. 6, the phenomenon is more obvious in Fig. 8. For designs corresponding to L=50 mm, two initially surprising characteristics develop. The first is the emergence of what appear to be notches in the region above the re-entrant corner, although they are likely better characterized as *fins*, as we subsequently explain. The second corresponds to the additional *fin-like* features that primarily appear on the structural members in the lower left region of the design domain.²⁰ The optimizer wishes to both reduce the amount of material and constrain $\bar{\epsilon}$ in regions where it exceeds its upper bound. One manner in which the optimizer can exploit the mathematical model, is to create regions which are largely unloaded (in comparison to the nearby primary structure) into which $\bar{\epsilon}$ may diffuse in order to lower the peak magnitude in the region. This phenomenon appears independent of the structural member size, as demonstrated in Appendix E. Although, experiments are clearly needed to confirm/deny this claim, it seems that when the ratio $L/\ell_{\bar{\epsilon}}$ is "sufficiently small", the optimizer often exploits the mathematical model in a way that is no longer consistent with the physics it was originally intended to approximate.

Additionally, this behavior is also explicitly manifest in the region near the re-entrant corner, as highlighted in Fig. 11. Although it is initially surprising that the optimizer does not completely remove the re-entrant corner in the case of brittle or quasi-brittle material design, it is clear that keeping at least an $\ell_{\bar{\epsilon}}$ radius of material around the corner enables more diffusion of $\bar{\epsilon}$, consequently lowering its peak magnitude. Therefore, the amount of the re-entrant corner that is retained is directly related to the parameter $\ell_{\bar{\epsilon}}$. For fixed $\ell_{\bar{\epsilon}}$, this causes the appearance of more re-entrant corner removal *relative* to the size of domain, L. Note that the same behavior is observed for all considered values of ω and $\bar{\epsilon}_{max}$. Many of topology optimization works mentioned in the introduction that consider gradient-enhanced damage during the optimization procedure provide examples where re-entrant corners are not completely removed. Although there could be other contributing factors, the ratio of domain size to the length scale of the gradient-enhanced quantity should be considered. A few examples correspond to $L/\ell_{\bar{\epsilon}}$ approximately in the range of 20-50 which generally leads to very diffuse damage regions. In these cases, re-entrant corner removal may not result since the gradient-enhanced quantity driving damage is reduced when there is additional material present around the corner into which it may diffuse.

¹⁹ The effect of r_{\min} is further explored in Appendix E.

 $^{^{20}}$ Increasing the penalty exponent on the parameter c amplifies this effect as shown in Fig. 22 in Appendix D.

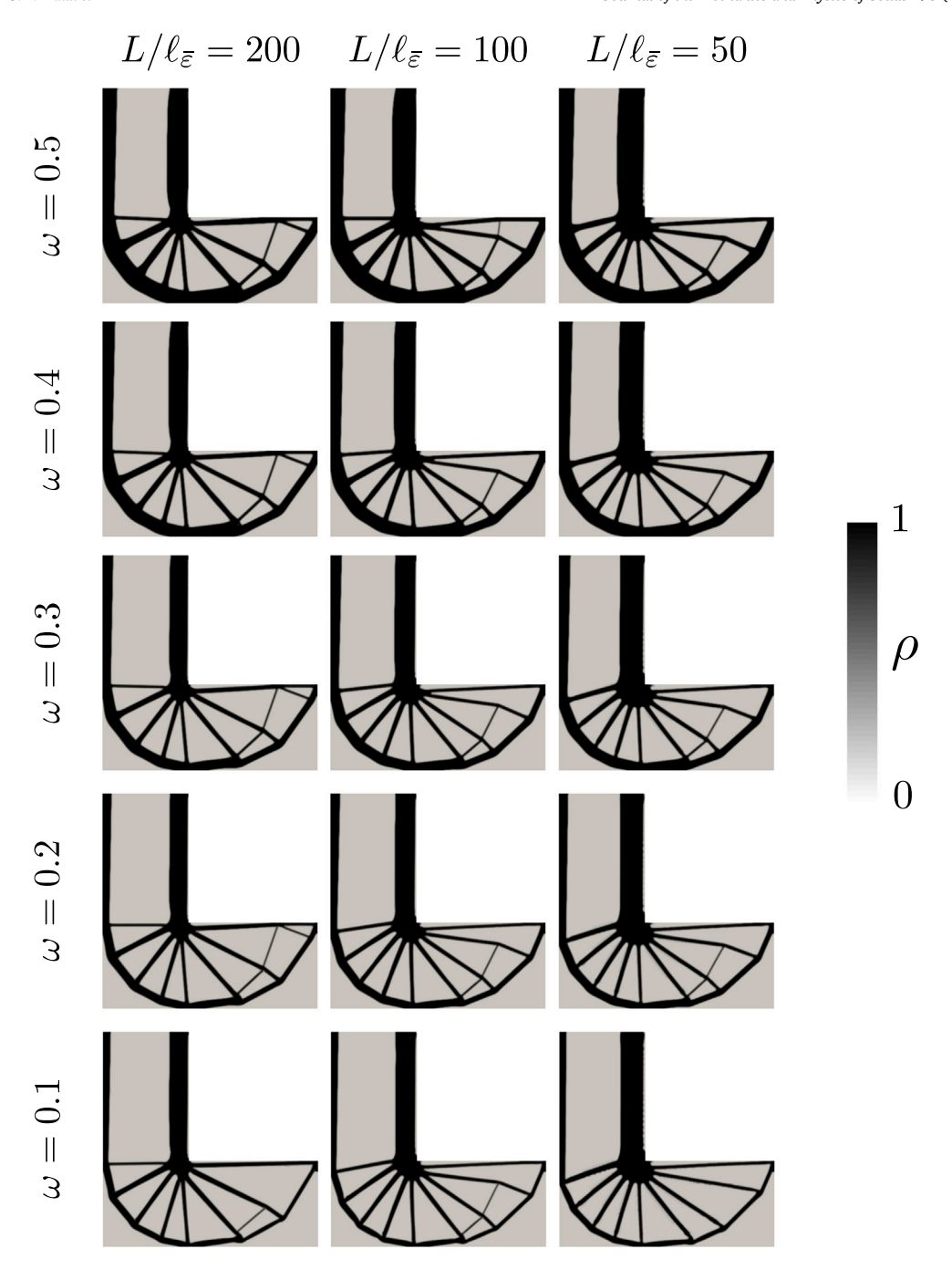


Fig. 6. Optimized density fields for the L-bracket corresponding to each weighting parameter (ω) and domain size (L), all with local constraint upper bound, $\bar{\epsilon}_{\max} = \kappa_0$.

5.2. Portal frame example

The portal frame example provides contrast to the L-bracket due to the difference in loading mode (i.e., primarily mode I vs. mixed mode) and the smaller proportion of the domain which is subject to high tensile loading. In particular, the right-most vertical column of the L-bracket must endure a large tensile load in addition to the re-entrant corner itself. On the other hand, the portal frame is characterized by a stronger stress singularity at the re-entrant corner, albeit without such a large region of comparably high tensile loading. Perhaps unsurprisingly, this leads to some differences in the observed behavior. In the following examples, the

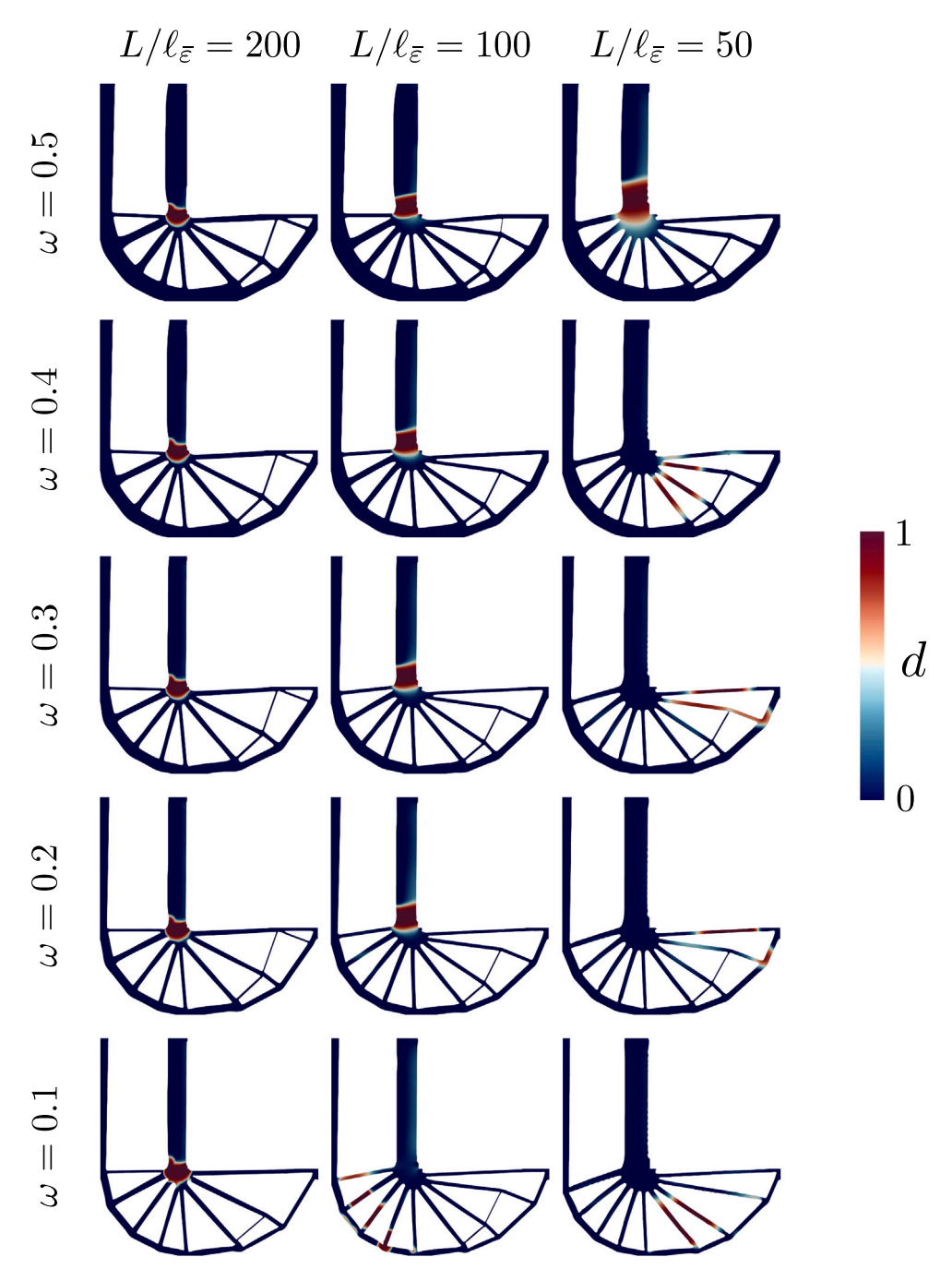


Fig. 7. Damage fields corresponding to post-optimization verification simulations of the load capacity for each optimized design presented in Fig. 6.

filter radii for the three design domains are consistently scaled with L, resulting in r_{\min} values of 8 mm, 4 mm, and 2 mm. Identical values of $\bar{\epsilon}_{\max}$ are explored (i.e., κ_0 and $0.95 \times \kappa_0$) and the same procedure is followed as for the L-bracket.

The results corresponding to $\bar{\epsilon}_{max} = \kappa_0$ are provided first, with optimized topologies shown in Fig. 12 and corresponding damage field predictions in Fig. 13.²¹ The relevant mechanical properties predicted post-optimization in each case are provided in Table 6,

 $^{^{21}}$ Each set of five designs obtained for each domain size (L) required \approx 4.2 hours running on 4 MPI ranks of a workstation consisting of an Intel Xeon® Gold 6258R CPU and 192 GB of RAM. The corresponding individual nonlinear damage simulations (i.e., those during post-optimization verification) each required less than 25 min to execute.

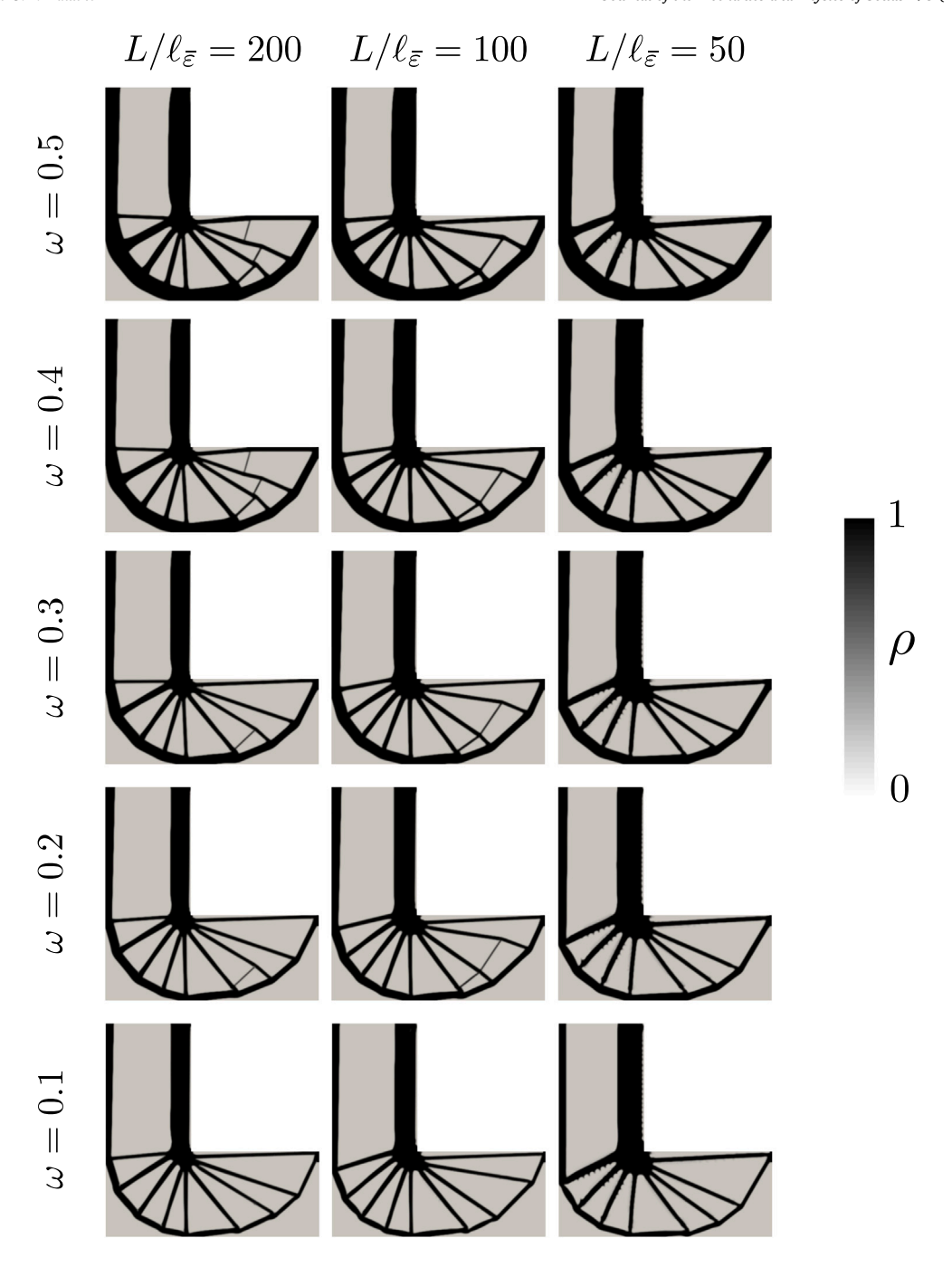


Fig. 8. Optimized density fields for the L-bracket corresponding to each weighting parameter (ω) and domain size (L), all with local constraint upper bound, $\bar{\epsilon}_{\max} = 0.95 \times \kappa_0$.

including the peak load capacity, volume fraction, and the end displacement at 90% of the design load. Additionally, the results corresponding to the tighter upper bound on the gradient-enhanced strain measure (i.e., $\bar{\epsilon}_{max} = 0.95 \times \kappa_0$) are provided in Figs. 14, 15, and Table 7. All force vs. displacement curves are collected into Fig. 16, in which the design load level is also clearly illustrated for each domain size, L. This figure highlights the fact that *all* designs satisfy the load capacity requirement, including those corresponding to the smallest design domain (i.e., L = 50 mm). Similar to the L-bracket, decreasing the upper bound $\bar{\epsilon}_{max}$ produces designs with higher load capacity.

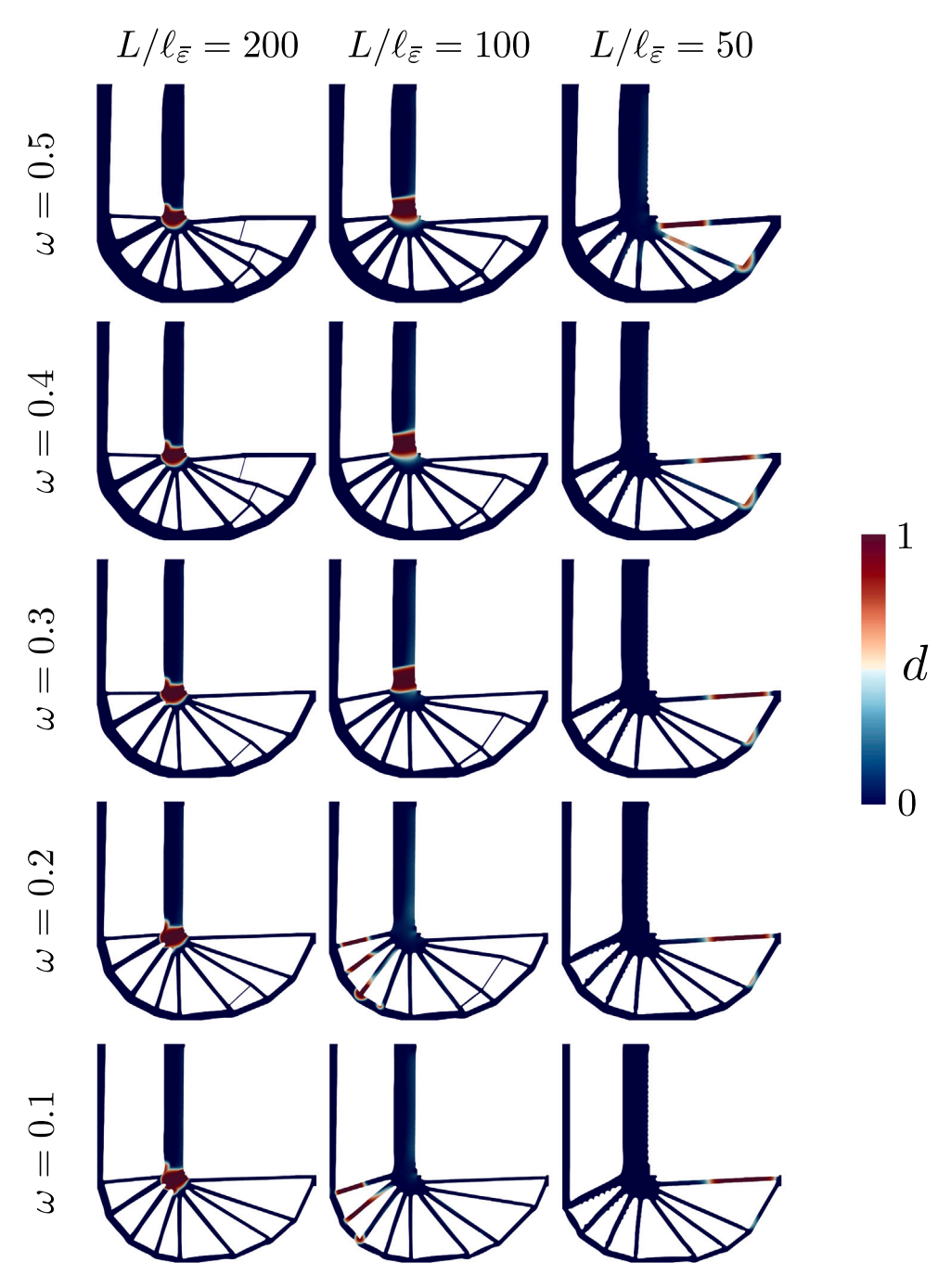


Fig. 9. Damage fields corresponding to post-optimization verification simulations of the load capacity for each optimized design presented in Fig. 8.

Interestingly, the "fin-like" patterns, which appeared in several L-bracket examples, are absent from the portal frame designs. However, as is shown in Fig. 17, the behavior near the re-entrant corner is nearly identical in character to that of the L-bracket example. Again, to diffuse as much $\bar{\epsilon}$ away from the re-entrant corner as possible, all material within a radius of at least $\ell_{\bar{\epsilon}}$ is retained. Therefore, when the domain size L is small relative to $\ell_{\bar{\epsilon}}$, it appears as though the optimizer does not wish to get rid of the re-entrant corner. A more appropriate characterization of this observation might be that the optimizer exploits the mathematical model to satisfy the local constraints. Notice that this fundamental behavior underlies other topology optimization formulations using similar gradient-enhanced damage models. Consequently, similar behavior near re-entrant corners should be expected in many of these cases. The question remains, is this representative of the physics or is it simply an artifact of the mathematical model?

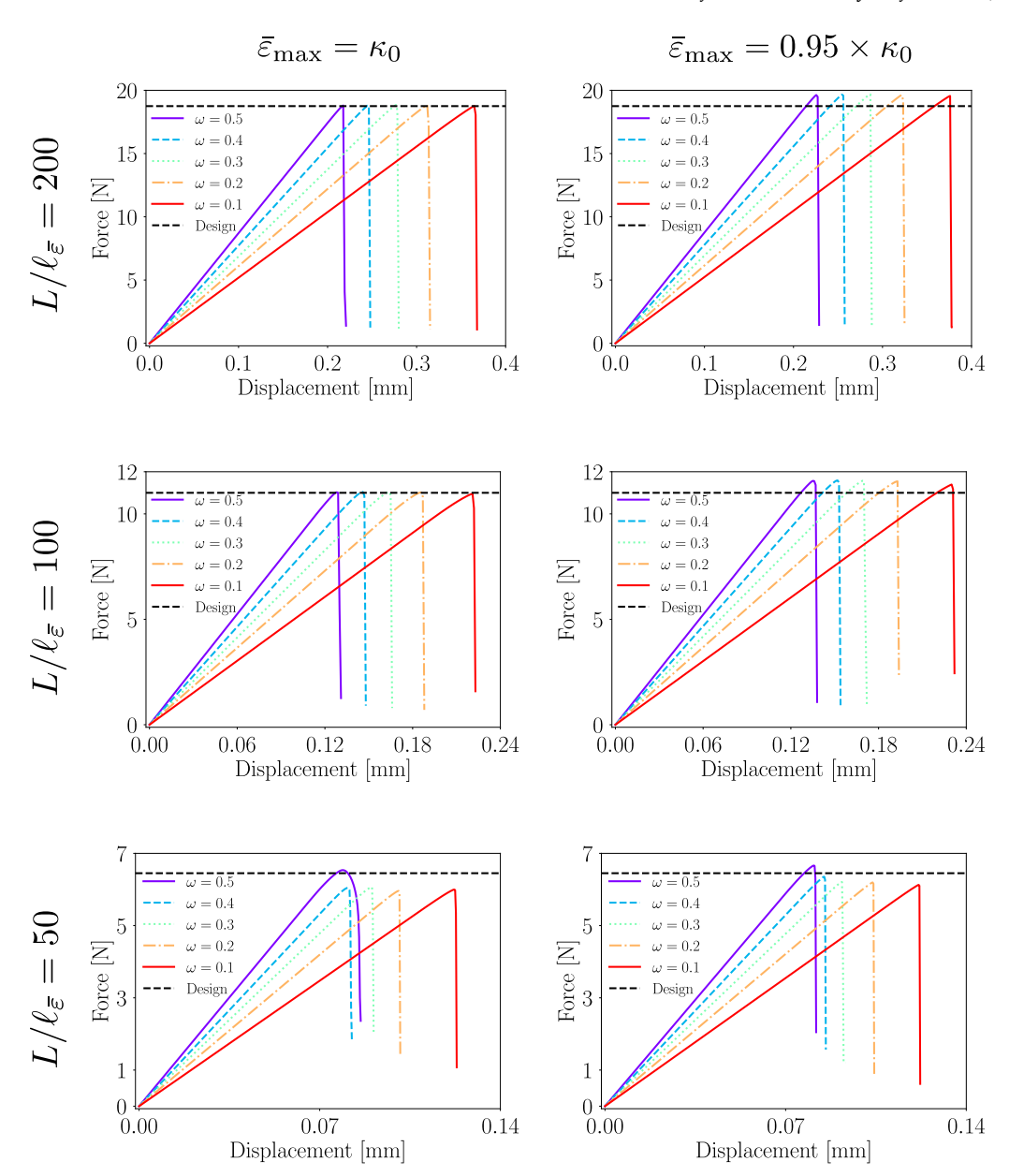


Fig. 10. Force vs. displacement curves obtained from post-optimization verification simulations of all presented L-bracket designs.

Table 6 Portal frame post-optimization verification results obtained for $\bar{\epsilon}_{\max} = \kappa_0$. The volume fraction (VF), peak load capacity (PL), and the end displacement (U) are reported. Note that U corresponds to the end displacement at 90% of the design load for each domain size (L).

ω	L = 200 mm			L = 100 mm			L = 50 mm		
	VF	PL [N]	U [mm]	VF	PL [N]	U [mm]	VF	PL [N]	U [mm]
0.5	0.430	26.963	0.067	0.435	16.122	0.041	0.428	9.637	0.026
0.4	0.368	25.273	0.077	0.370	14.967	0.047	0.362	9.241	0.030
0.3	0.303	24.453	0.092	0.306	14.747	0.056	0.307	9.192	0.035
0.2	0.244	24.158	0.113	0.248	14.837	0.069	0.252	9.083	0.042
0.1	0.191	24.225	0.146	0.197	14.826	0.088	0.208	8.990	0.052

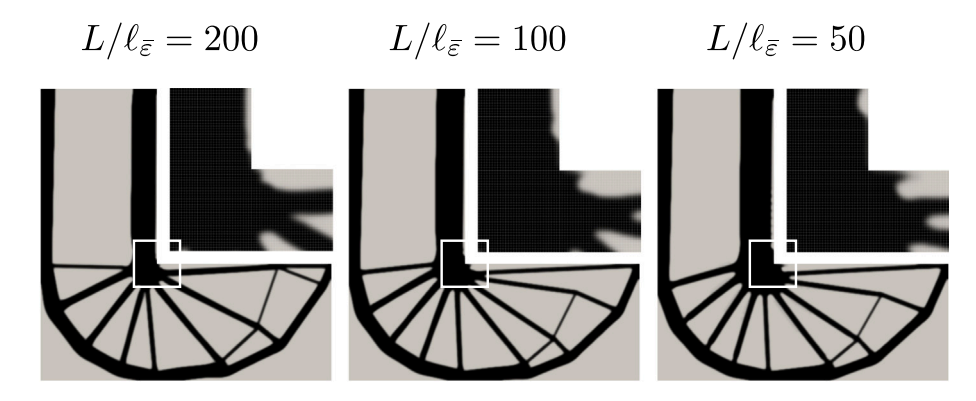


Fig. 11. L-bracket optimized designs corresponding to $\omega = 0.3$, and $\bar{\varepsilon}_{\max} = \kappa_0$. An enlarged view near the re-entrant corner (corresponding to the white box) is shown for each domain size, illustrating the effect of L relative to the length scale $\ell_{\bar{\varepsilon}}$ near the re-entrant corner.

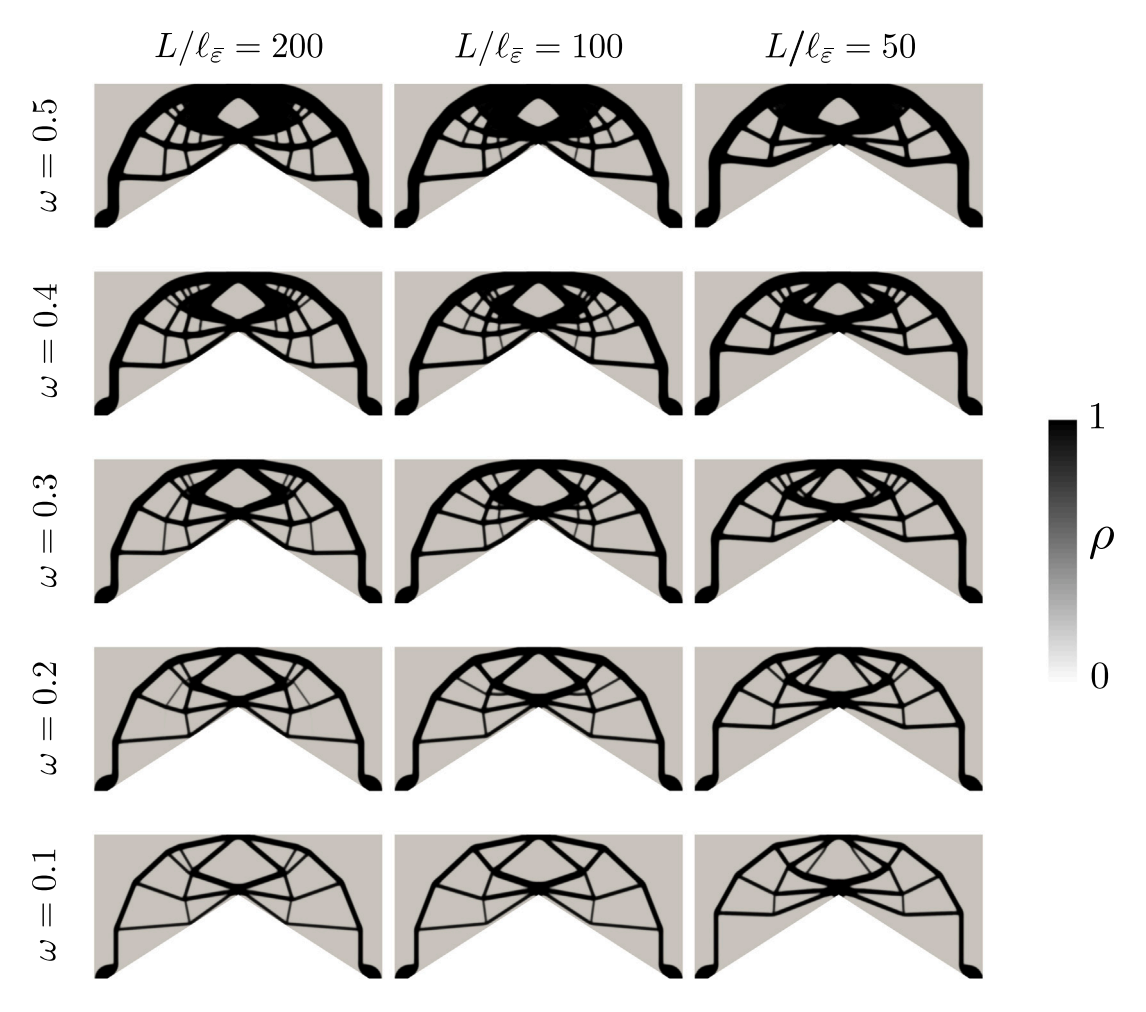


Fig. 12. Optimized density fields for the portal frame corresponding to each weighting parameter (ω) and domain size (L), all with local constraint upper bound, $\bar{\epsilon}_{\max} = \kappa_0$.

6. Concluding remarks

A basic topology optimization procedure based on linear physics is presented, providing a set of optimized designs with a user-defined load capacity and a trade-off between mass and stiffness. The key insight stems from examination of the mathematical form of a sufficiently accurate failure model for the material of interest (assuming one currently exists). This often enables determination of

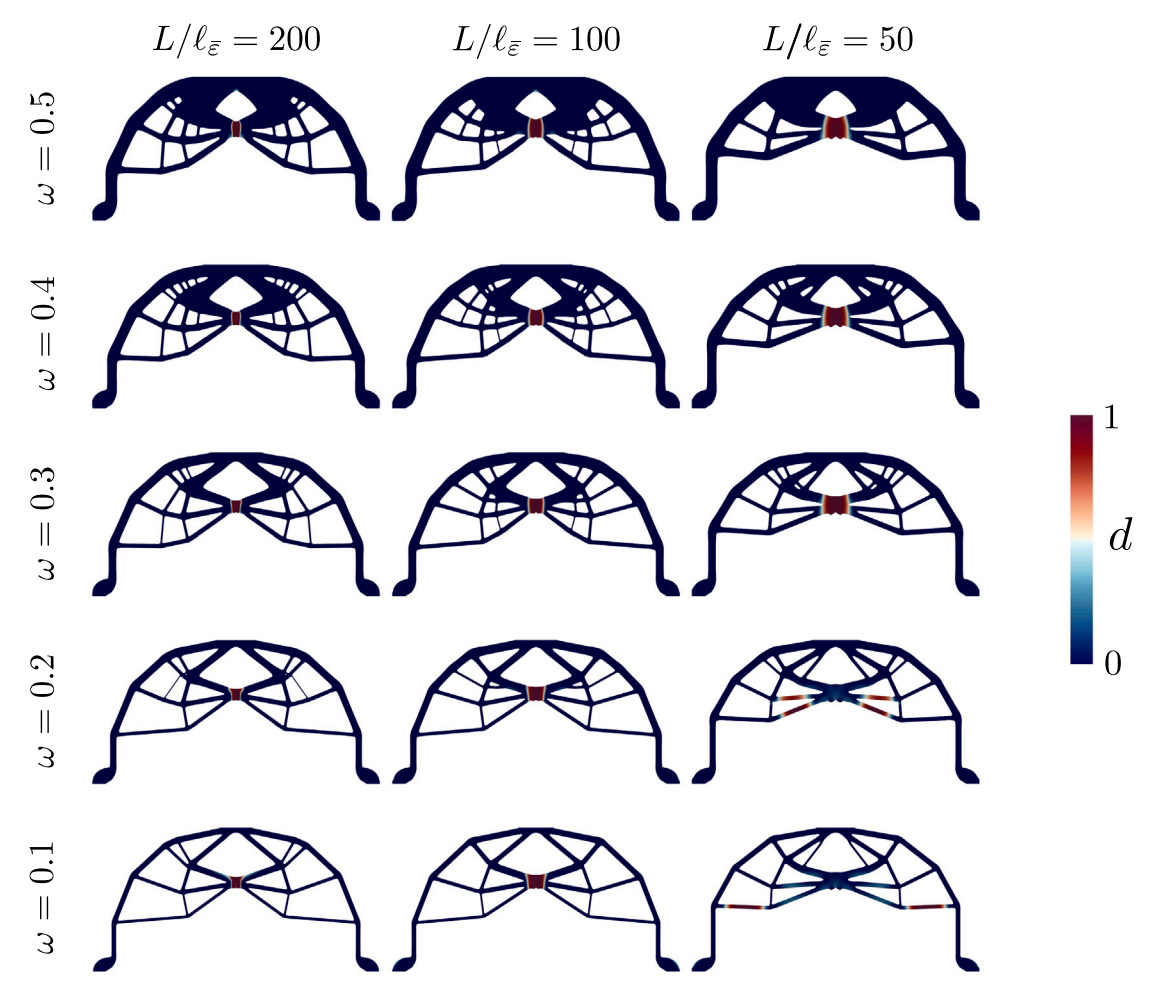


Fig. 13. Damage fields corresponding to post-optimization verification simulations of the load capacity for each optimized design presented in Fig. 12.

Table 7 Portal frame post-optimization verification results obtained for $\bar{\epsilon}_{\max} = 0.95 \times \kappa_0$. The volume fraction (VF), peak load capacity (PL), and the end displacement (U) are reported. Note that U corresponds to the end displacement at 90% of the design load for each domain size (L).

ω	L = 200 mm			L = 100 1	L = 100 mm			L = 50 mm		
	VF	PL [N]	U [mm]	VF	PL [N]	U [mm]	VF	PL [N]	U [mm]	
0.5	0.435	27.702	0.067	0.432	16.385	0.041	0.427	9.922	0.026	
0.4	0.370	26.561	0.078	0.360	15.590	0.048	0.367	9.660	0.030	
0.3	0.305	25.413	0.092	0.303	15.549	0.056	0.309	9.632	0.035	
0.2	0.246	25.101	0.113	0.247	15.506	0.069	0.258	9.409	0.042	
0.1	0.196	25.028	0.144	0.204	15.460	0.086	0.216	9.440	0.051	

both the useful quantity to constrain at each integration point and an approximate upper bound to impose. Although we have shown only results corresponding to a standard gradient-enhanced damage model, the idea can be generalized to other failure models, including most recent phase-field fracture formulations. The mechanical performance of each optimized structure is evaluated via post-optimization verification simulations, which are uncoupled from the optimization process and are unaffected by the density field and material parameter interpolation schemes. This enables higher fidelity simulations of the relevant physics and perhaps a better assessment of what may be necessary to capture during the optimization process in order to improve design performance, if desired.

The user-specified design load level for each problem is directly applied to the structure during each optimization problem. By constraining the damage driving force to be lower than the threshold for damage initiation, one indirectly assures that at the design (i.e. applied) load level, very little damage has accumulated. The parameter ω controls the trade-off between stiffness and mass but does not have a significant, direct impact on the peak value of the gradient-enhanced strain measure which is subject to the same

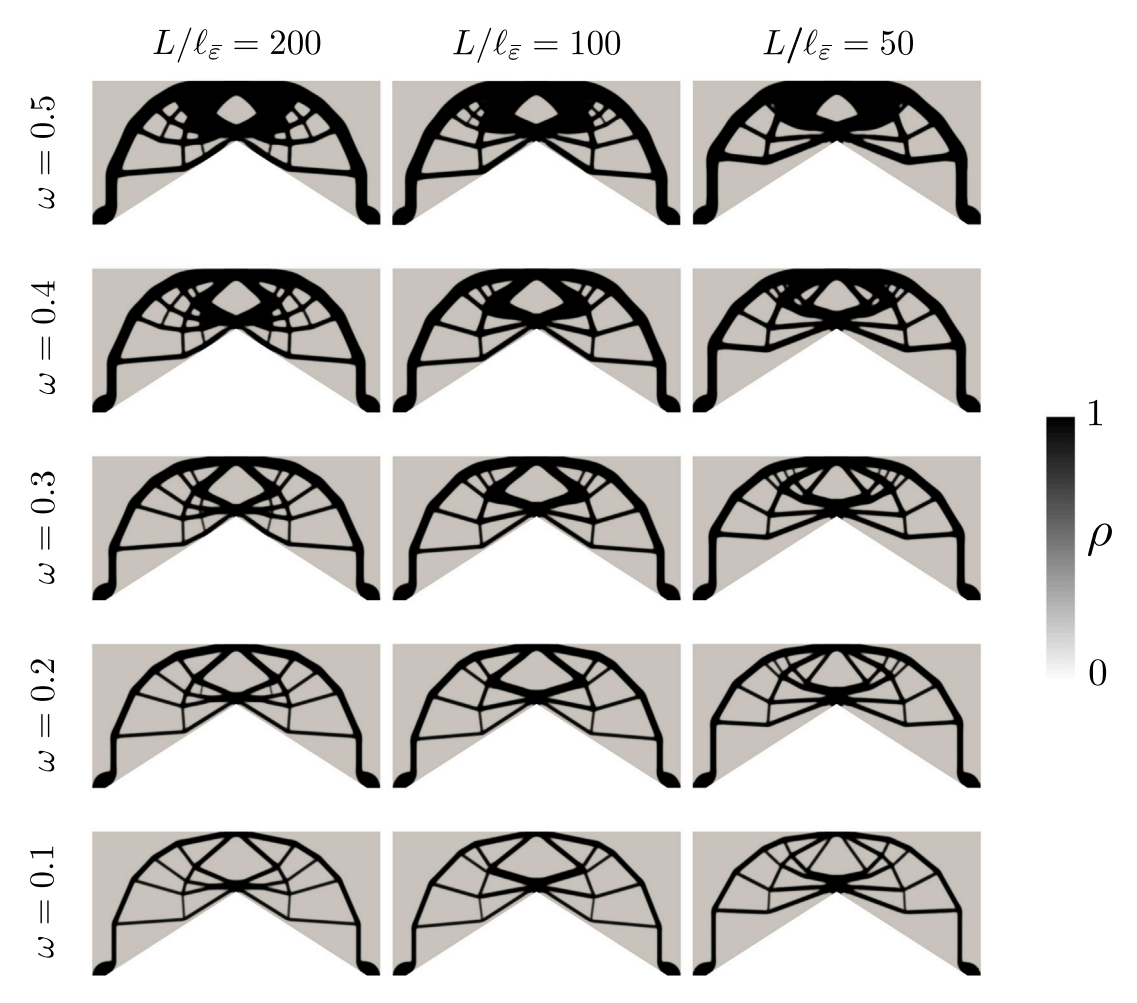


Fig. 14. Optimized density fields for the portal frame corresponding to each weighting parameter (ω) and domain size (L), all with local constraint upper bound, $\bar{\epsilon}_{\max} = 0.95 \times \kappa_0$.

upper bound throughout the domain. Since the onset of damage corresponds to the situation in which the local gradient-enhanced strain has exceeded the threshold value, if the constraints are satisfied at the design (i.e., applied) load level, then the structure should at least be capable of supporting this load level without failure. This places an indirect lower-bound on the load capacity, equal to the applied load (assuming of course that the no-flux boundary condition is sufficiently enforced internal to the design domain as previously discussed). The L-bracket results generally demonstrate that complete structural failure occurs quite rapidly once this threshold is exceeded and damage initiates. However, the implicit lower bound on the load capacity is approached from above for most of the portal frame examples as the parameter ω is reduced, due in part to the steady reduction of material. This implies that for larger values of ω it is possible for the load capacity to be significantly higher than the design load, hence the adoption of the proposed continuation scheme on the parameter ω , which systematically produces a sequence of designs approaching the design load capacity due to the increased importance placed on reducing the quantity of material.

Due to the use of linear physics during the optimization procedure, the formulation is sufficiently robust and numerically efficient for use in engineering practice where multiple load cases are ubiquitous and computational resources/time are often limited. Of further importance in many industries, the proposed method could readily be extended to dynamic load cases, while remaining free from the usual requirement of displacement-controlled loading, as is currently the case for existing topology optimization formulations that consider the failure physics explicitly during the optimization process.

For the specific class of gradient-enhanced damage models in which the quantity driving damage evolution is regularized (e.g., the one considered in this work) rather than the damage parameter itself (e.g., phase-field fracture), a few interesting observations emerge. We summarize these observations here, many of which appear to be symptoms of the mathematical model used to approximate the relevant physics. However, such a determination would best be made via a set of carefully designed experiments.

• When $L/\ell_{\bar{\ell}}$ is small (i.e., approximately ≤ 100), optimized designs typically retain re-entrant corners where $\bar{\epsilon}$ is generally $\geq \bar{\epsilon}_{max}$. A solid region of radius $\ell_{\bar{\epsilon}}$ or greater around such corners will usually remain to aid in constraint satisfaction via

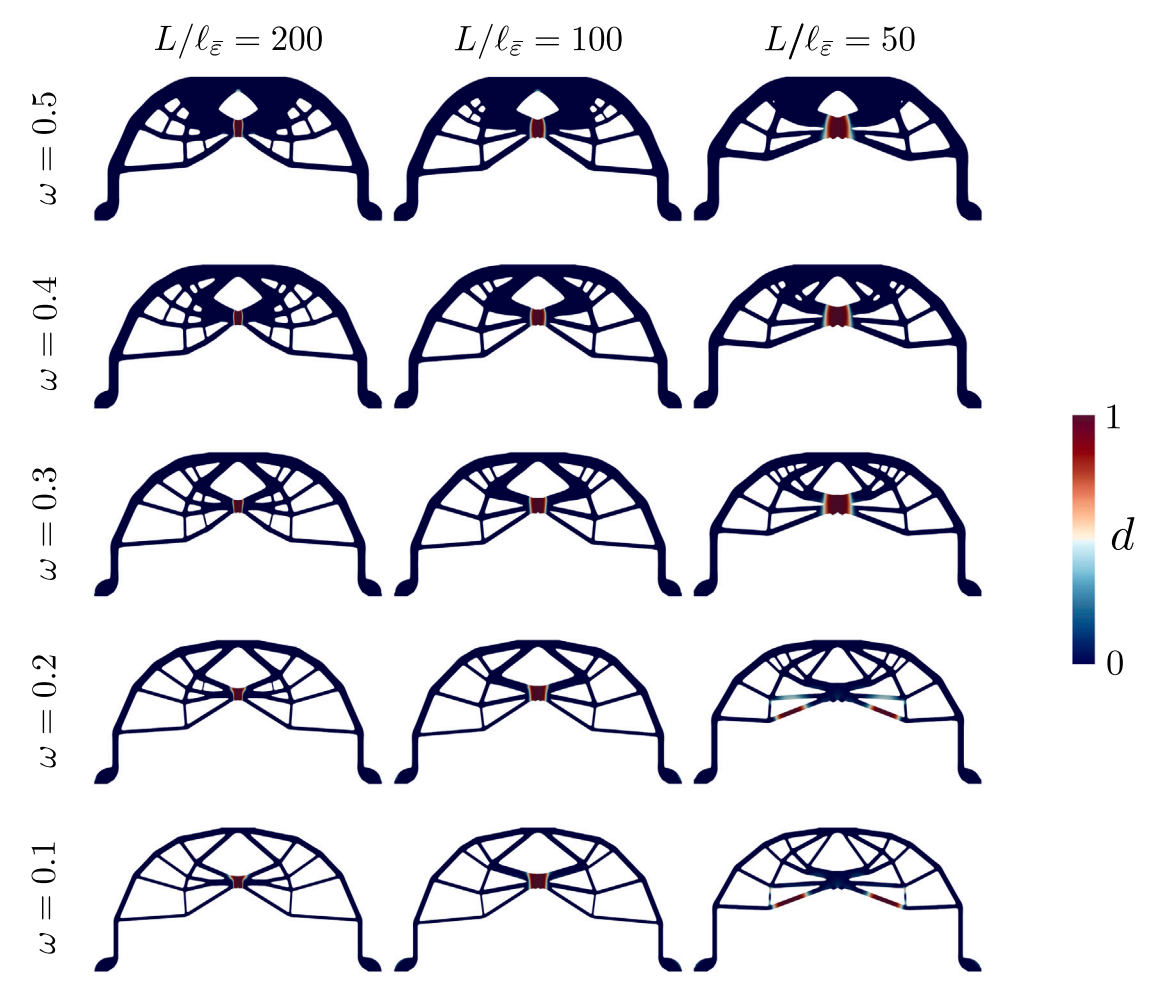


Fig. 15. Damage fields corresponding to post-optimization verification simulations of the load capacity for each optimized design presented in Fig. 14.

diffusion. Additionally, "fin-like" patterns may develop on structural members in optimized designs. These features typically serve as regions with lower values of ε_{eq} into which the optimizer can locally diffuse larger values that are present within a distance of $\ell_{\bar{e}}$. This phenomenon appears to be independent of the filter radius, r_{\min} .

• When the structural member size is small relative to $\ell_{\tilde{e}}$ (e.g., when $r_{\min}/\ell_{\tilde{e}} < 2$), it is beneficial to increase the penalization exponent in the interpolation function for the parameter c. This enables better enforcement of the no-flux boundary condition present in the boundary value problem and helps produce designs with the desired load capacity. Please note the relevant discussion at the end of Appendix D.

Finally, we wish to emphasize that the proposed procedure works well when crack/damage nucleation is of interest; *not* propagation. The majority of the existing topology optimization formulations that explicitly model damage during the optimization process result in optimized designs in which the magnitude and extent of damage is very small when subject to the loading applied *during* the optimization procedure. This is especially true when the magnitude of the damage variable is constrained explicitly. In most situations, these small damage regions likely do not have a strong impact on the quantities of interest that are constrained or extremized, making it unlikely that explicit damage simulation during the optimization process is significantly beneficial. Furthermore, in the surprisingly common case when the length scale, $\ell_{\bar{\epsilon}}$ is chosen to be so large that only *very* diffuse regions of damage (of similar size to the design domain) are predicted, it seems as though the physics of the problem are no longer accurately approximated. This does, however, make the topology optimization problem much easier to solve since it generally corresponds with a mechanical response that is gentler in the softening regime and also enables the use of a coarser finite element mesh. In sharp contrast, larger ratios of $L/\ell_{\bar{\epsilon}}$ lead to increasingly brittle physics, intense damage evolution, and finer required discretizations; all of which pose nontrivial challenges for gradient-based optimization with many design variables. Although our proposed formulation does not address the ill-conditioned, but practically relevant case, of topology optimization with crack/damage *propagation*, it does provide a useful, extensible methodology for *preventing* structural failure that can be implemented and tested against more complex, numerically expensive formulations.

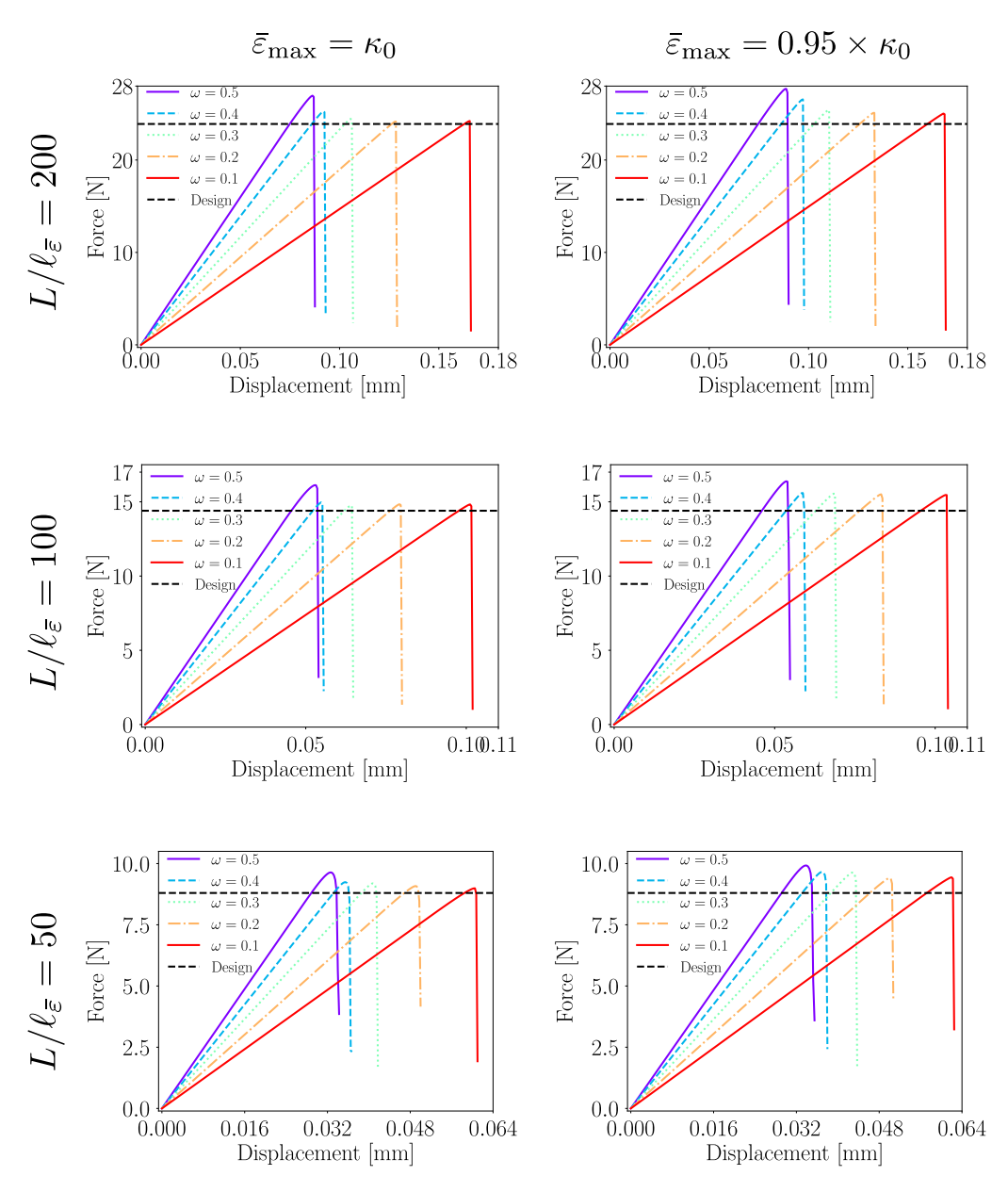


Fig. 16. Force vs. displacement curves obtained from post-optimization verification simulations of all presented portal frame designs.

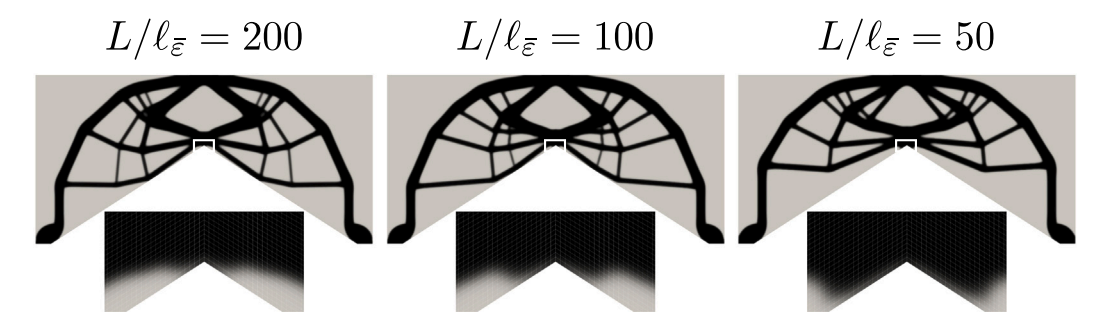


Fig. 17. Portal frame optimized designs corresponding to $\omega = 0.3$, and $\bar{\epsilon}_{\max} = \kappa_0$. An enlarged view near the re-entrant corner (corresponding to the white box) is shown for each domain size, illustrating the effect of L relative to the length scale $\ell_{\tilde{\epsilon}}$ near the re-entrant corner.

CRediT authorship contribution statement

Jonathan B. Russ: Conceptualization, Methodology, Software, Writing – original draft, Writing – review & editing. **Glaucio H. Paulino:** Conceptualization, Methodology, Writing – review & editing, Supervision, Funding acquisition, Resources.

Declaration of competing interest

The authors declare that they have no known competing financial interests or personal relationships that could have appeared to influence the work reported in this paper.

Data availability

To facilitate replication of the results, the paper discusses the formulation in detail and provides the input parameters for each of the numerical examples.

Acknowledgment

This work was partially funded by the National Science Foundation, United States (NSF) through grant #2105811.

Replication of results

To facilitate replication of the results, the paper discusses the formulation in detail and provides all the input parameters for each of the numerical examples.

Appendix A. Damage formulation used for post-optimization verification

The isotropic gradient-enhanced continuum damage formulation of Peerlings et al. (1996) used for verification of the load capacity of the optimized designs is briefly summarized in this section. The gradient-enhanced quantity, $\bar{\epsilon}$, introduced in Section 3 is used to drive the evolution of a local history parameter, κ , through the KKT conditions $\dot{\kappa} \geq 0$, $\bar{\epsilon} - \kappa \leq 0$, and $\dot{\kappa}(\bar{\epsilon} - \kappa) = 0$. Using κ , the damage variable, $d \in [0, 1]$, is then computed locally at a material point according to Mazars and Pijaudier-Cabot (1989),

$$d(\kappa) = 1 - \frac{\kappa_0}{\kappa} \left(1 - \alpha + \alpha \ e^{-\beta(\kappa - \kappa_0)} \right) \tag{A.1}$$

where α and β are fitting parameters which should be calibrated using experimental data and κ is initialized to κ_0 , which represents the threshold at which damage evolution begins. Furthermore, due to the well-known loss of ellipticity of the governing equations, a monolithic solution via a typical Newton iteration can be challenging in the softening regime. Therefore, a viscous damage evolution law (Simo and Ju, 1987),

$$\dot{d}_v = \frac{1}{n} \left(d - d_v \right) \tag{A.2}$$

is used in order to achieve controlled convergence during the post-optimization verification simulations of the optimized topologies. Taking η sufficiently small, one may obtain a forward solution that is nearly indistinguishable from the inviscid case. However, this facilitates a numerically converged result in the softening regime by significantly reducing the pseudo-time increment. Using this viscous damage, the Cauchy stress tensor may then be expressed,

$$\sigma = (1 - d_n) \,\mathbb{C}_0 : \varepsilon \tag{A.3}$$

which is distinguished from the stress tensor used in the linear formulation (i.e., Eq. (3.3)). Utilizing a fully implicit time discretization of Eq. (A.2) and the evolution of κ at a material point, we obtain

$$\kappa^n = \max\left(N_{\varepsilon}\bar{\epsilon}^n, \, \kappa^{n-1}\right) \tag{A.4}$$

$$d_v^n = \frac{1}{1+m} d_v^{n-1} + \frac{m}{1+m} d(\kappa^n), \text{ where } m \equiv \frac{\Delta t}{\eta}$$
(A.5)

where the superscript $(\cdot)^n$ implies the quantity is evaluated at pseudo-time t^n and Δt represents a pseudo-time increment. The applied displacement in each post-optimization verification analysis is linearly ramped and a pseudo-time of 1 corresponds to the applied displacement at the peak load capacity in each of the fully dense simulations illustrated in Figs. 3 and 4. Near the peak load capacity, Δt is decreased from 10^{-2} to 10^{-4} seconds and the analysis is continued until a fully-developed damage region is observed.

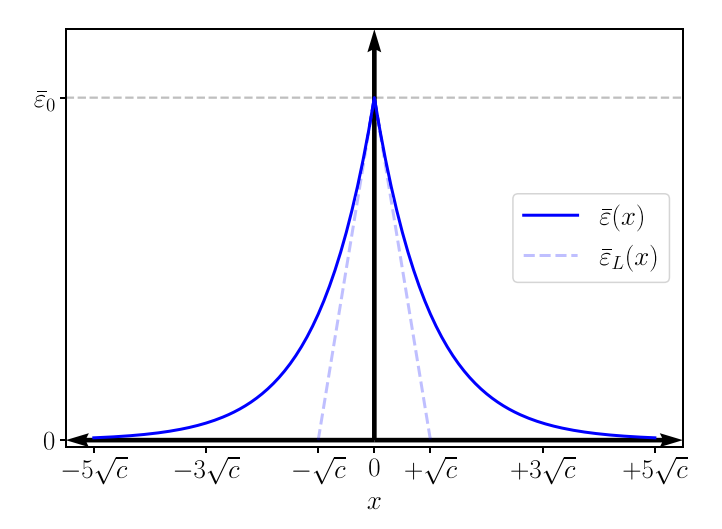


Fig. 18. One dimensional homogeneous solution of Eq. (3.8) briefly illustrating an approximate relationship between the gradient-enhanced strain and the parameter, c. Note that $\bar{\epsilon}(x)$ represents the analytical solution whereas $\bar{\epsilon}_I(x)$ corresponds to its first-order Taylor expansion about x=0 (obtained for $x\in\mathbb{R}^\pm$ separately).

Appendix B. Relationship between c and $\ell_{\bar{\epsilon}}$

For reader convenience, we briefly illustrate the approximate relationship between the parameter c and the length scale $\ell_{\bar{t}}$ associated with the gradient-enhanced strain measure $\bar{\epsilon}$. Note that this follows a mathematically identical derivation to that shown for many of the earlier phase-field fracture models (e.g., Miehe et al., 2010). In one space dimension where $x \in [-\infty, \infty]$, we may solve the homogeneous form of Eq. (3.8), subject to the boundary conditions that $\bar{\epsilon}(x=0) = \bar{\epsilon}_0$ and $\bar{\epsilon}(x=\pm\infty) = 0$. This produces the well-known analytical solution, $\bar{\varepsilon}(x) = \bar{\varepsilon}_0 \exp\left(-\frac{|x|}{\sqrt{c}}\right)$. A first-order Taylor expansion of this solution about x=0 (treating $x\in\mathbb{R}^\pm$ separately) results in the approximation $\bar{\varepsilon}_L(x) = \bar{\varepsilon}_0\left(1-\frac{|x|}{\sqrt{c}}\right)$. Both of these functions are illustrated in Fig. 18. One may define the gradient-enhanced strain length scale $(\ell_{\bar{\varepsilon}})$ in many ways but two common approaches are as follows:

- 1. Set $\ell_{\bar{\varepsilon}}$ to half the width of the domain in which $\bar{\varepsilon}_L(x) \geq 0$, corresponding to $\ell_{\bar{\varepsilon}} \equiv \sqrt{c} \implies c = \ell_{\bar{\varepsilon}}^2$ 2. Set $\ell_{\bar{\varepsilon}}$ to the full width of the domain in which $\bar{\varepsilon}_L(x) \geq 0$, corresponding to $\ell_{\bar{\varepsilon}} \equiv 2\sqrt{c} \implies c = \frac{1}{4}\ell_{\bar{\varepsilon}}^2$

In this work, we proceed with the former convention and set $c = \mathcal{C}_{\varepsilon}^2$.

Appendix C. Constraining $\bar{\epsilon}$ versus ϵ_{eq}

When the length scale, $\ell_{\bar{e}}$, is small relative to the size of the design domain, there is little difference between ϵ_{eq} and \bar{e} , as implied by Eq. (3.8). In this case, one could simply constrain the local quantity, ϵ_{eq} , using only linear elastic physics. However, if $\ell_{\bar{e}}$ is not small relative to the domain size, then it frequently becomes necessary to include the solution of the gradient-enhanced counterpart in the formulation.²² Consider the following one-dimensional boundary value problem corresponding to Eqs. (3.8) and (3.9).

$$-\ell_{\bar{\varepsilon}}^2 \frac{d^2 \bar{\varepsilon}}{dx^2} + \bar{\varepsilon} = \varepsilon_{eq} \text{ for } x \in [-10, 10] \text{ with } \frac{d\bar{\varepsilon}}{dx} \Big|_{x=-10} = \frac{d\bar{\varepsilon}}{dx} \Big|_{x=10} = 0$$
 (C.1)

Taking $\varepsilon_{eq}(x) \equiv 1$, it is easily verified that $\bar{\varepsilon}(x) = \varepsilon_{eq}(x) \ \forall x \in [-10, \ 10]$ regardless of $\ell_{\bar{\varepsilon}}$. However, taking the simple piece-wise linear "hat" function $\epsilon_{eq}(x) = \max(1 - |x|, 0)$ and noting that L = 20, Fig. 19 illustrates how the gradient-enhanced strain can differ from the equivalent strain depending on $L/\ell_{\bar{e}}$. Since most strain fields are inhomogeneous, this simple example provides the intuition behind the observed behavior for the L-bracket example subsequently presented in this section. Namely, as $L/\ell_{\bar{\ell}}$ becomes smaller, the peak values of $\bar{\epsilon}$ compared to those of ϵ_{eg} generally become significantly smaller. Therefore, placing the same upper bound on ε_{eq} can easily result in local constraints that become increasingly difficult to satisfy (except in the rare case of a homogeneous strain field). However, as $L/\ell_{\bar{e}}$ increases, the peak value of \bar{e} approaches that of ϵ_{eq} from below, resulting in local constraints that are generally decreasingly conservative.

²² Importantly, this is only a characteristic of gradient-enhanced damage models in which the damage driving force is regularized (via the introduction of a length scale) rather than the damage parameter itself. Consequently, phase-field fracture models (e.g., Miehe et al., 2010) do not suffer from this issue and only linear elastic physics need be used, typically with local constraints on the tensile strain energy density.

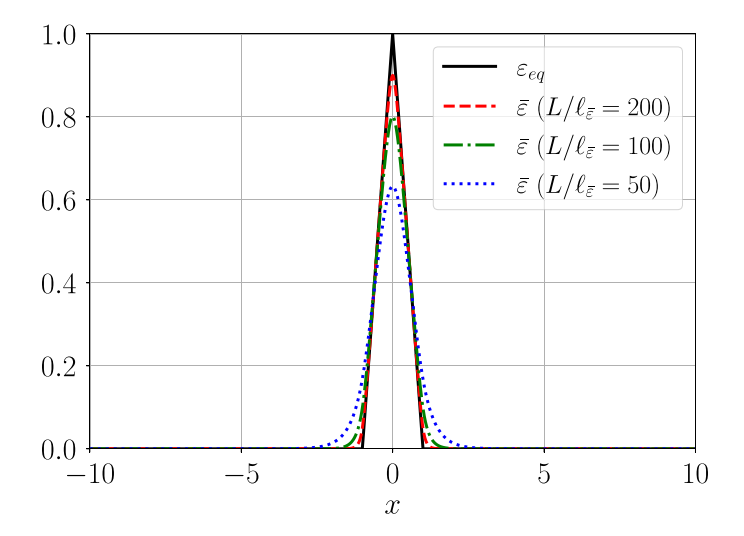


Fig. 19. An illustration of multiple solutions to Eq. (C.1) when compared with the driving force, ε_{eq} .

Here we take the L-bracket example from Section 5.1, and solve the modified optimization problem shown in Eq. (C.2) in which the equivalent strain is constrained and only linear elastic physics are required.

$$\min_{\boldsymbol{z} \in [0,1]^{N_{elem}}} \omega \frac{f_{ext}^T \underline{\boldsymbol{u}}}{f_{ext}^T \underline{\boldsymbol{u}}} + (1 - \omega) \frac{\rho^T V}{\rho_0^T V}$$
s.t. $\epsilon_{eq}(\boldsymbol{x}_{e_q}) \le \kappa_0$, $e = 1, \dots, N_{elem}$, $q = 1, \dots, N_{quad}$
with: $\boldsymbol{R}_{\boldsymbol{u}}(\boldsymbol{\rho}, \boldsymbol{u}) = \boldsymbol{0}$

A single weighting parameter of $\omega=0.5$ is considered which adequately demonstrates the potential impact on the optimized result when compared with the results obtained utilizing the formulation defined in Eq. (4.1) with $\bar{\epsilon}_{\rm max}=\kappa_0$. The resulting optimized designs are compared for L=200 mm and L=100 mm in Fig. 20. Although the formulation corresponding to Eq. (4.1) is able to obtain a feasible result for L=50 mm, constraining the equivalent strain results in an optimization problem with no feasible design obtained after 600 iterations. The design obtained for L=100 mm demonstrates much more material is required to satisfy the local constraints (volume fraction of 0.604 versus 0.423; a 42.8% increase in material). However, when L=200 mm, the volume fraction of the optimized designs are significantly closer, as expected, although the design corresponding to Eq. (C.2) is still more conservative, requiring more material (i.e., volume fraction 0.430 versus 0.407; a 5.6% increase in material) and exhibiting a peak load capacity greater than that of the proposed formulation and the specified load capacity. These results seem to suggest that design problems in which $L/\ell_{\bar{\ell}}$ is approximately greater than 200 may facilitate the use of either formulation without risk of generating overly conservative designs. However this should only be taken as a "rule-of-thumb" since, like most rules, there are inevitably exceptions. The implications of this are quite interesting since the formulation to use significantly depends not only on the material being used ($\ell_{\bar{\ell}}$) but also on the scale of the design problem (L). Again, we refer the interested reader to the beginning of Bažant (2004) for a broad range of fracture process zone sizes across a wide variety of materials of interest. Therefore, the designer must be keenly aware of these two scales when selecting a design algorithm for their particular application.

Finally, we note two additional important observations. The first is that the linear solve required for the gradient-enhanced strain is generally much cheaper than that of the linear elasticity problem since the matrix is smaller by a factor of 1 over the space-dimension, while also remaining symmetric and positive-definite. However, the introduction of a length-scale requires the resolution of $\nabla \bar{\epsilon}$, implicitly placing an upper bound on the finite element size (approximately $h < \ell_{\bar{\epsilon}}/2$, where h represents the typical element size, assuming first-order basis functions are used). For problems in which $L/\ell_{\bar{\epsilon}} > 200$ this may not be an issue since Eq. (C.2) is likely sufficient, however for other design problems this may significantly increase the solution time depending on whether a much finer discretization is required to accurately approximate $\nabla \bar{\epsilon}$ in the solid region (i.e., $\rho \approx 1$) due to the magnitude of $\ell_{\bar{\epsilon}}$.

Appendix D. Effect of the penalization $\chi_c(\rho_e)$

As previously highlighted and briefly discussed in Section 5.1, the penalization exponent in the interpolation function used for the parameter c can have a large impact on the effectiveness of the formulation to produce designs which meet the desired load capacity. In this section we briefly demonstrate this for the smallest domain size (i.e., L=50 mm) in which the problem is most clearly manifest (as evidenced by the results shown in Fig. 10). All parameters and procedures are identical with the exception of the penalization function, $\chi_c(\rho_e)$, for which we provide results corresponding to the 3 choices. The first $(\chi_c(\rho_e)=1)$ corresponds

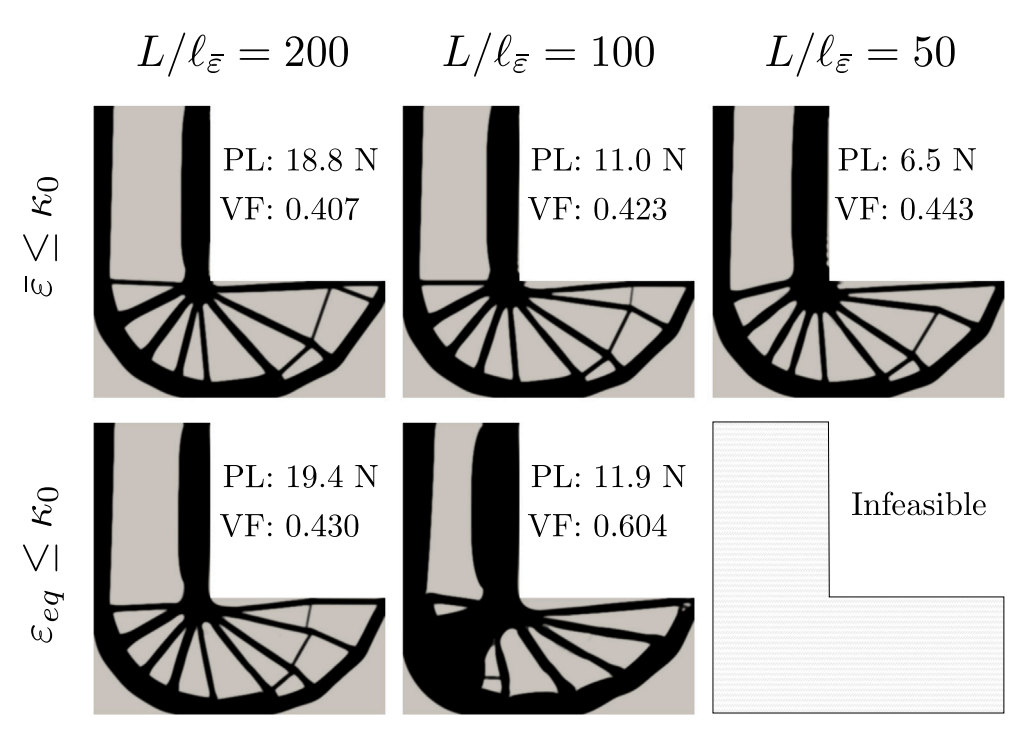


Fig. 20. L-bracket optimized design comparison between Eq. (4.1) with $\bar{\epsilon} \leq \kappa_0$ and Eq. (C.2) with $\epsilon_{eq} \leq \kappa_0$, for each domain size (*L*). The volume fraction (VF) and peak load capacity (PL) for each design is also provided. The results in the first row correspond to those previously presented in Fig. 6.

to no penalization or interpolation of c, the second $(\chi_c(\rho_e) = \rho_e)$ corresponds to the results presented in Section 5.2, and the third $(\chi_c(\rho_e) = \rho_e^p)$ corresponds to penalization p equivalent to that of the elastic modulus (including the associated continuation on this parameter from 1 to 3). The optimized topologies for each case are illustrated in Fig. 22, with subsequently computed damage fields provided in Fig. 23, and the relevant numerical data presented in Table 8. Fig. 23 demonstrates the change in failure location when $\chi_c(\rho_e) = \rho_e^p$ is used, and most strikingly we find from Fig. 21(c) that this corresponds to achievement of the design load capacity for all ω . Fig. 21(a) further demonstrates that no penalization of this parameter leads to designs which are far from being able to support the design load.

These results highlight that when $L/\ell_{\bar{\epsilon}}$ is small (particularly when $r_{\min}/\ell_{\bar{\epsilon}}$ is not sufficiently greater than 1 as shown in Appendix E), special care must be demonstrated when selecting an appropriate penalty for the parameter c. Additionally, this implies the existence of an implicit lower bound on the size of the design domain relative to $\ell_{\bar{\epsilon}}$ that is reasonable to use within this framework. Intuitively, this corresponds with the physical situation in which the design domain is not significantly larger than the "internal material length scale", likely requiring a different mathematical model to accurately approximate the relevant physics. Furthermore, note that taking $r_{\min} < \ell_{\bar{\epsilon}}$ makes little physical sense since it implies an acceptable structural member size smaller than that of the characteristic length scale of the material. This point is also mentioned in the work of James and Waisman (2014).

Finally, we wish to clearly state our reasoning for not taking $\chi_c(\rho_e) = \rho_e^p$ in every presented example in this work. While, this choice does generally increase the nonlinearity of the optimization problem in the design variables, the continuation scheme placed on the exponent (identical to that of the elastic modulus) does indeed appear to help alleviate some of this nonlinearity and would not fully justify taking $\chi_c(\rho_e) = \rho_e$, in general. Rather, our reasoning is two-fold. (1) Examining the results presented in column 2 and 3 of Fig. 22, it is clear that the increased penalty exponent exacerbates the appearance of the "fin-like" patterns previously mentioned, which we suspect are a spurious exploitation of the mathematical model rather than a feature relevant to the physics. (2) The large penalization exponent seems to only be required in special cases where the size of the design domain is not significantly larger than the material length scale. In these situations, we believe the designer should carefully consider the validity of numerical model. However, since meeting the design load capacity for the portal frame example with $L/\ell_{\tilde{e}} = 50$ was not an issue using $\chi_c(\rho_e) = \rho_e$, and we did not observe the emergence of "fin-like" patterns in the optimized results, we prefer to recommend the smallest effective interpolation penalty exponent that should suffice for *most* problems. We include this section to alert the reader of this potentially undesirable phenomenon in case it is encountered in practice.

As a simple "rule-of-thumb", for situations in which $r_{\min} \geq 2\ell_{\bar{e}}$ is not an acceptable or desirable option, the standard interpolation function (i.e., $\chi_c(\rho_e) = \rho_e$) should first be employed. However, if the resulting designs do not meet the load capacity requirement, then the designer may proceed with $\chi_c(\rho_e) = \rho_e^p$ in which the exponent is subject to the same continuation scheme as the elastic modulus.

Table 8

L-bracket post-optimization verification results obtained for the smallest domain size ($L=50~\mathrm{mm}$) and $\bar{\epsilon}_{\mathrm{max}}=\kappa_0$ with different interpolation functions for the parameter c. The volume fraction (VF), peak load capacity (PL), and the end displacement (U) are reported. Note that in this case U corresponds to the end displacement at a load of 3 N which all optimized structures were able to achieve. This provides a consistent, intuitive measure of compliance since many of these designs do not meet the original load capacity requirement.

ω	$\chi_c(\rho_e) = 1$			$\chi_c(\rho_e) = \rho$	$\chi_c(\rho_e) = \rho_e$			$\chi_c(\rho_e) = \rho_e^p$		
	VF	PL [N]	U [mm]	VF	PL [N]	U [mm]	VF	PL [N]	U [mm]	
0.5	0.438	5.396	0.035	0.443	6.536	0.035	0.450	6.622	0.035	
0.4	0.382	4.787	0.040	0.392	6.046	0.039	0.404	6.596	0.038	
0.3	0.335	4.245	0.046	0.354	6.065	0.044	0.372	6.582	0.043	
0.2	0.292	3.802	0.054	0.324	5.961	0.050	0.344	6.579	0.048	
0.1	0.240	3.386	0.071	0.296	5.997	0.060	0.318	6.587	0.058	

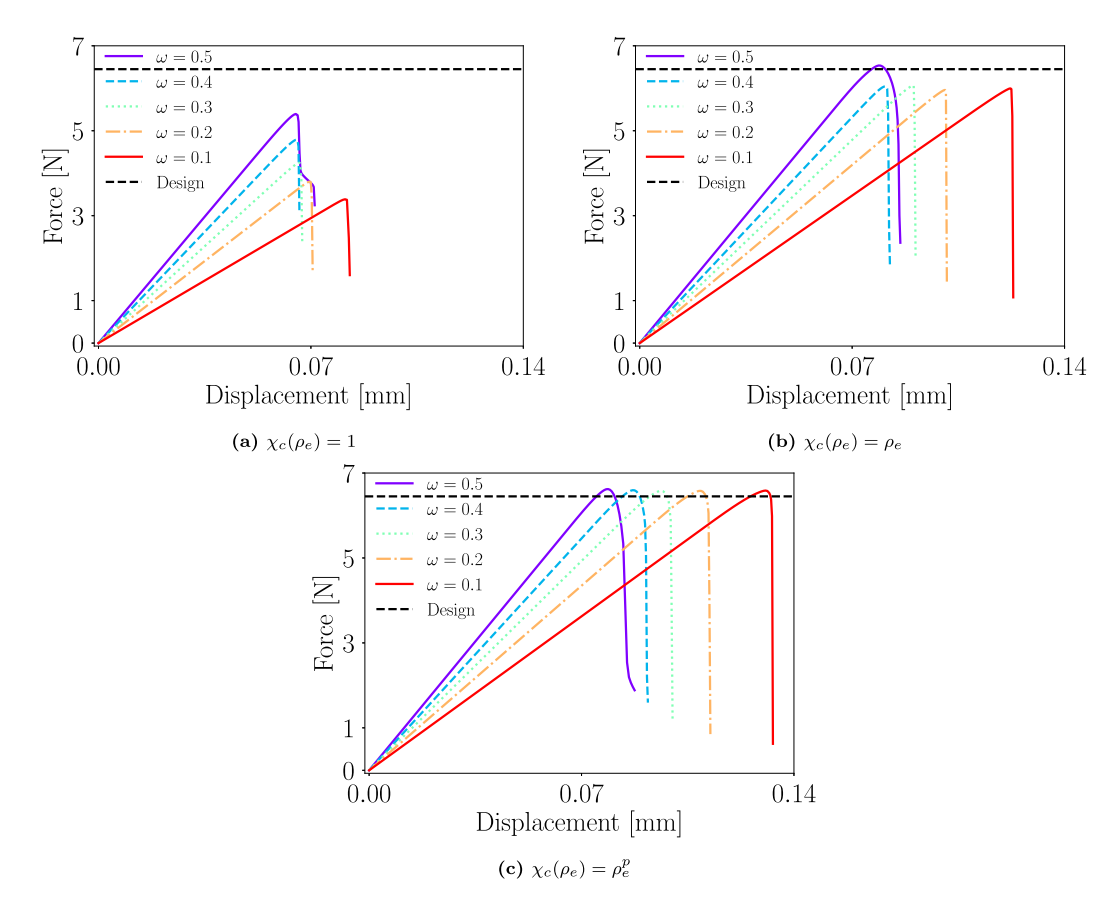


Fig. 21. Force vs. displacement curves obtained from post-optimization verification simulations of the L-bracket designs presented in this section corresponding to different penalizations of the parameter c. All results are obtained for L=50 mm and $\bar{\varepsilon}_{\rm max}=\kappa_0$.

Appendix E. Effect of the filter radius, r_{\min}

In Appendix D, it is demonstrated that there is a large effect of parameter c's interpolation when $L/\ell_{\bar{e}}$ is small (e.g., $L/\ell_{\bar{e}} = 50$ in this example). As also indicated in the aforementioned appendix, the filter radius (i.e., r_{\min}) also affects the whether the final design meets the load capacity requirement. The results for the smallest design domain (i.e., L = 50 mm) provided in Section 5.1 and Appendix D all correspond to a filter radius of $r_{\min} = 1$ mm (i.e., $r_{\min}/\ell_{\bar{e}} = 1$. In this section we double the filter radius (i.e., $r_{\min} = 2$ mm $\Rightarrow r_{\min}/\ell_{\bar{e}} = 2$) and provide the results, following the same procedure outlined in Appendix D. Table 9 contains the numerical data corresponding to each of the resulting designs illustrated in Fig. 25. The force versus displacement curves for each penalization function, $\chi_c(\rho_e)$, are shown in Fig. 24 with illustrations of the corresponding final damage fields provided in Fig. 26.

There are many interesting observations one could note from the results, however we highlight only the three we view as most important for clarity. First, Fig. 24(b) illustrates that choosing a larger filter radius in this example does indeed provide designs which satisfy the load capacity requirement using the original interpolation function, $\chi_c(\rho_e) = \rho_e$, without additional penalization. Second, this comes at the cost of increased volume fraction since the structural member sizes are generally larger. For example, considering

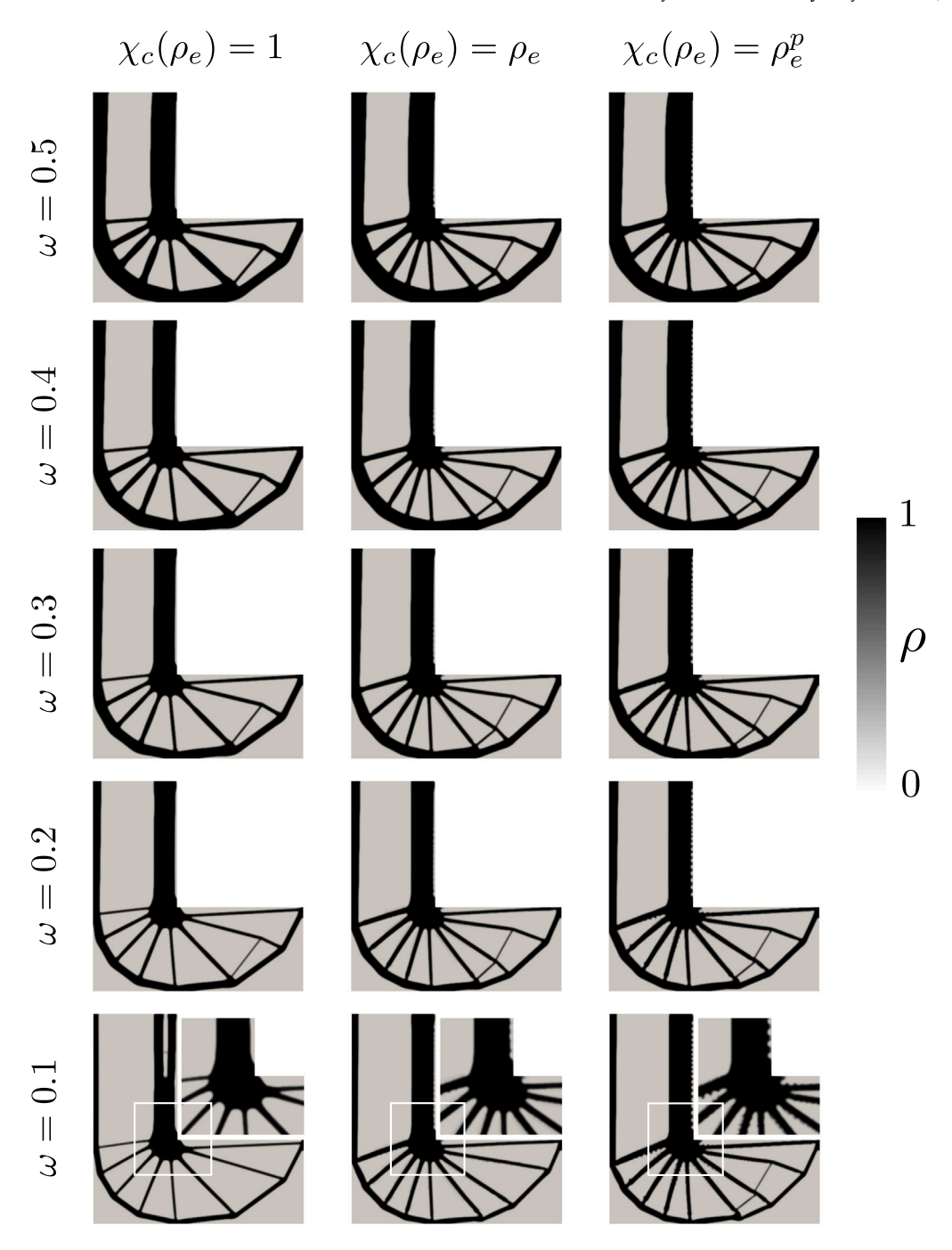


Fig. 22. Optimized topologies corresponding to different interpolations of the parameter c, the smallest L-bracket domain size considered (i.e., L=50 mm), and $\bar{\epsilon}_{\max}=\kappa_0$. An enlarged view near the re-entrant corner (corresponding to the white box) is shown for $\omega=0.1$ and each interpolation, demonstrating the emergence of the "fin-like" patterns.

only the lowest weight design in both Tables 8 and 9 which meet the load capacity requirement, a filter radius of $r_{\min}=1$ mm corresponds to a volume fraction of 0.318 versus the 0.431 obtained when $r_{\min}=2$ mm. A 26.2% reduction in volume fraction is certainly not trivial, therefore increasing the filter radius in order to meet the design load capacity is generally not advised. Third, and finally, note the appearance of the "fin-like" features on the large vertical member containing the re-entrant corner and the large member in the lower left region of the design domain. Again, these features occasionally appear in designs obtained with interpolation of the parameter c when $L/\ell_{\tilde{\epsilon}}$ is small. This example demonstrates that a larger filter radius (or larger structural member sizes, more generally) does not aid in the removal of these features. All previously mentioned results again highlight the

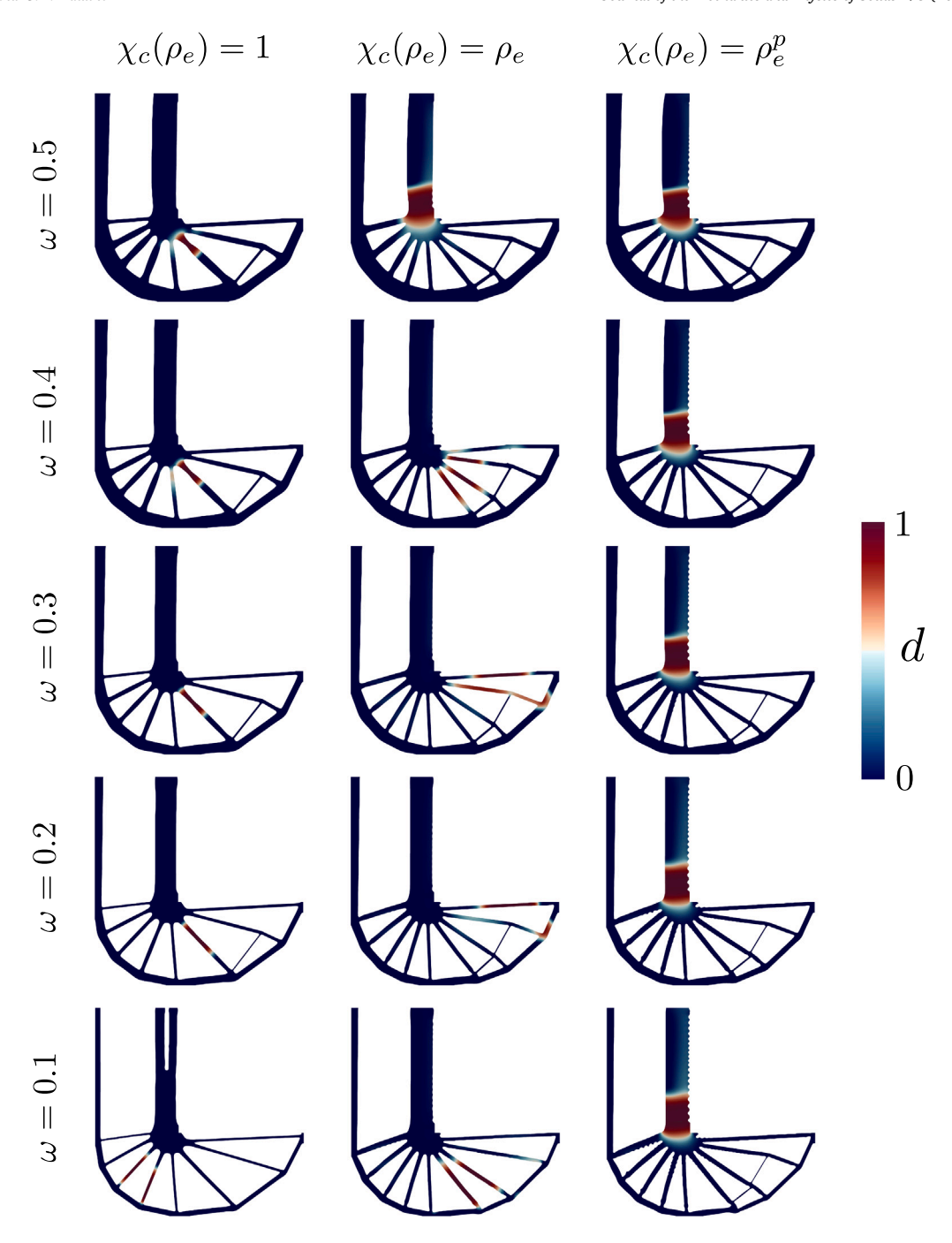


Fig. 23. Post-optimization verification simulation damage fields corresponding to the optimized topologies shown in Fig. 22.

relevant issues the designer must be aware of when using such a method to design structures that are not significantly larger than the characteristic internal length scale of the material.

Appendix F. Explicit derivatives & sensitivity verification

The analytical sensitivity analysis presented in Section 4.1 requires a few explicit derivatives to complete the derivation for the relevant function. Here those derivatives are provided along with a sensitivity verification analysis in which the result is compared

Table 9

L-bracket post-optimization verification results obtained for the smallest domain size (L=50 mm), $\bar{\epsilon}_{\rm max}=\kappa_0$, different interpolation functions for the parameter c, and double the original filter radius (i.e., $r_{\rm min}=2$ mm). The volume fraction (VF), peak load capacity (PL), and the end displacement (U) are reported. Note that in this case U corresponds to the end displacement at a load of 3 N which all optimized structures were able to achieve.

ω	$\chi_c(\rho_e) = 1$			$\chi_c(\rho_e) = \rho$	\mathcal{O}_e		$\chi_c(\rho_e) = \rho_e^p$		
	VF	PL [N]	U [mm]	VF	PL [N]	U [mm]	VF	PL [N]	U [mm]
0.5	0.469	6.522	0.034	0.530	6.872	0.033	0.553	7.002	0.033
0.4	0.418	6.165	0.038	0.494	6.696	0.036	0.517	6.983	0.035
0.3	0.374	5.817	0.042	0.472	6.714	0.039	0.495	6.958	0.037
0.2	0.341	5.551	0.047	0.458	6.873	0.041	0.477	6.980	0.040
0.1	0.314	5.481	0.055	0.446	6.875	0.044	0.431	6.625	0.046

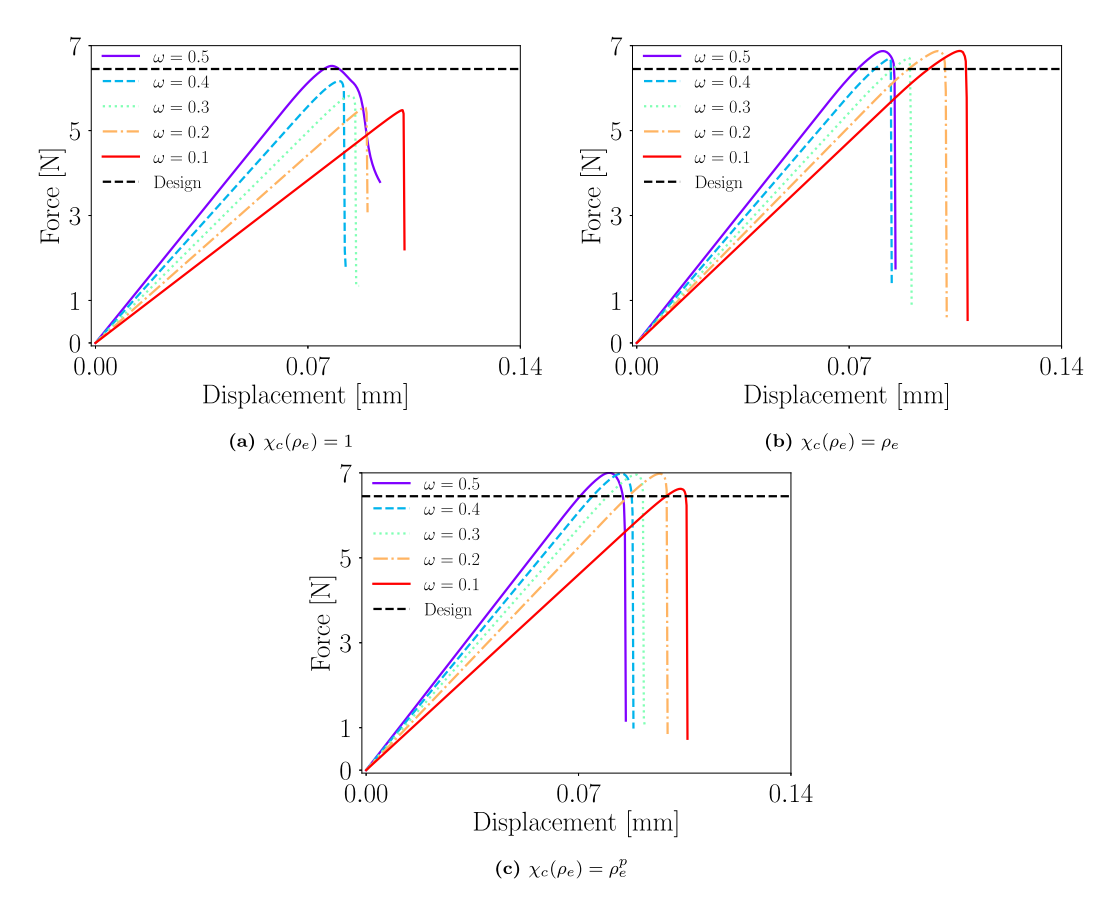


Fig. 24. Force vs. displacement curves obtained from post-optimization verification simulations of the L-bracket designs presented in this section, with different interpolations of the parameter c and double the original filter radius (i.e., $r_{\min} = 2$ mm). All results correspond to L = 50 mm and $\bar{\epsilon}_{\max} = \kappa_0$.

with a higher order finite difference scheme.

$$\begin{split} \frac{\partial \boldsymbol{R}_{\boldsymbol{u}}}{\partial \rho_{e}} &= \mathcal{A}_{e=1}^{N_{elem}} \sum_{q=1}^{N_{quad}} \frac{d \chi_{E}}{d \rho_{e}} \left(\boldsymbol{B}_{\boldsymbol{u}} : \mathbb{C}_{0} : \boldsymbol{\varepsilon}_{e_{q}} \right) \boldsymbol{w}_{e_{q}} & \frac{\partial \boldsymbol{R}_{\bar{\epsilon}}}{\partial \rho_{e}} = \mathcal{A}_{e=1}^{N_{elem}} \sum_{q=1}^{N_{quad}} \left[\frac{d \chi_{c}}{d \rho_{e}} c \; \boldsymbol{B}_{\bar{\epsilon}}^{T} \boldsymbol{B}_{\bar{\epsilon}} \underline{\boldsymbol{\xi}} - \frac{d \chi_{e_{eq}}}{d \rho_{e}} \; \boldsymbol{N}_{\bar{\epsilon}}^{T} \boldsymbol{\varepsilon}_{eq} \right] \boldsymbol{w}_{e_{q}} \\ \frac{\partial \boldsymbol{R}_{\boldsymbol{u}}}{\partial \boldsymbol{u}} &= \mathcal{A}_{e=1}^{N_{elem}} \sum_{q=1}^{N_{quad}} \chi_{E}(\rho_{e}) \left(\boldsymbol{B}_{\boldsymbol{u}} : \mathbb{C}_{0} : \boldsymbol{B}_{\boldsymbol{u}} \right) \boldsymbol{w}_{e_{q}} & \frac{\partial \boldsymbol{R}_{\boldsymbol{u}}}{\partial \underline{\boldsymbol{\xi}}} = \boldsymbol{0} \\ \frac{\partial \boldsymbol{R}_{\bar{\epsilon}}}{\partial \underline{\boldsymbol{u}}} &= \mathcal{A}_{e=1}^{N_{elem}} \sum_{q=1}^{N_{quad}} \left(-\chi_{\epsilon_{eq}}(\rho_{e}) \; \boldsymbol{N}_{\bar{\epsilon}}^{T} \frac{\partial \boldsymbol{\varepsilon}_{eq}}{\partial \boldsymbol{\varepsilon}} : \boldsymbol{B}_{\boldsymbol{u}} \right) \boldsymbol{w}_{e_{q}} & \frac{\partial \boldsymbol{R}_{\bar{\epsilon}}}{\partial \underline{\boldsymbol{\xi}}} = \mathcal{A}_{e=1}^{N_{elem}} \sum_{q=1}^{N_{quad}} \left[\chi_{c}(\rho_{e}) \; c \; \boldsymbol{B}_{\bar{\epsilon}}^{T} \boldsymbol{B}_{\bar{\epsilon}} + \boldsymbol{N}_{\bar{\epsilon}}^{T} \boldsymbol{N}_{\bar{\epsilon}} \right] \boldsymbol{w}_{e_{q}} \\ \frac{\partial \boldsymbol{f}}{\partial \rho_{e}} &= \sum_{q=1}^{N_{quad}} \left(\hat{\lambda}_{e_{q}}^{(\hat{k})} + \hat{\mu}_{e_{q}}^{(\hat{k})} h_{e_{q}}(\rho_{e}, \underline{\boldsymbol{\xi}}) \right) \frac{\partial h_{e_{q}}}{\partial \rho_{e}} & \frac{\partial \boldsymbol{f}}{\partial \underline{\boldsymbol{\xi}}} = \mathcal{A}_{e=1}^{N_{elem}} \sum_{q=1}^{N_{quad}} \left[\left(\hat{\lambda}_{e_{q}}^{(\hat{k})} + \hat{\mu}_{e_{q}}^{(\hat{k})} h_{e_{q}}(\rho_{e}, \underline{\boldsymbol{\xi}}) \right) \frac{\partial h_{e_{q}}}{\partial \underline{\boldsymbol{\xi}}} \right] \end{split}$$

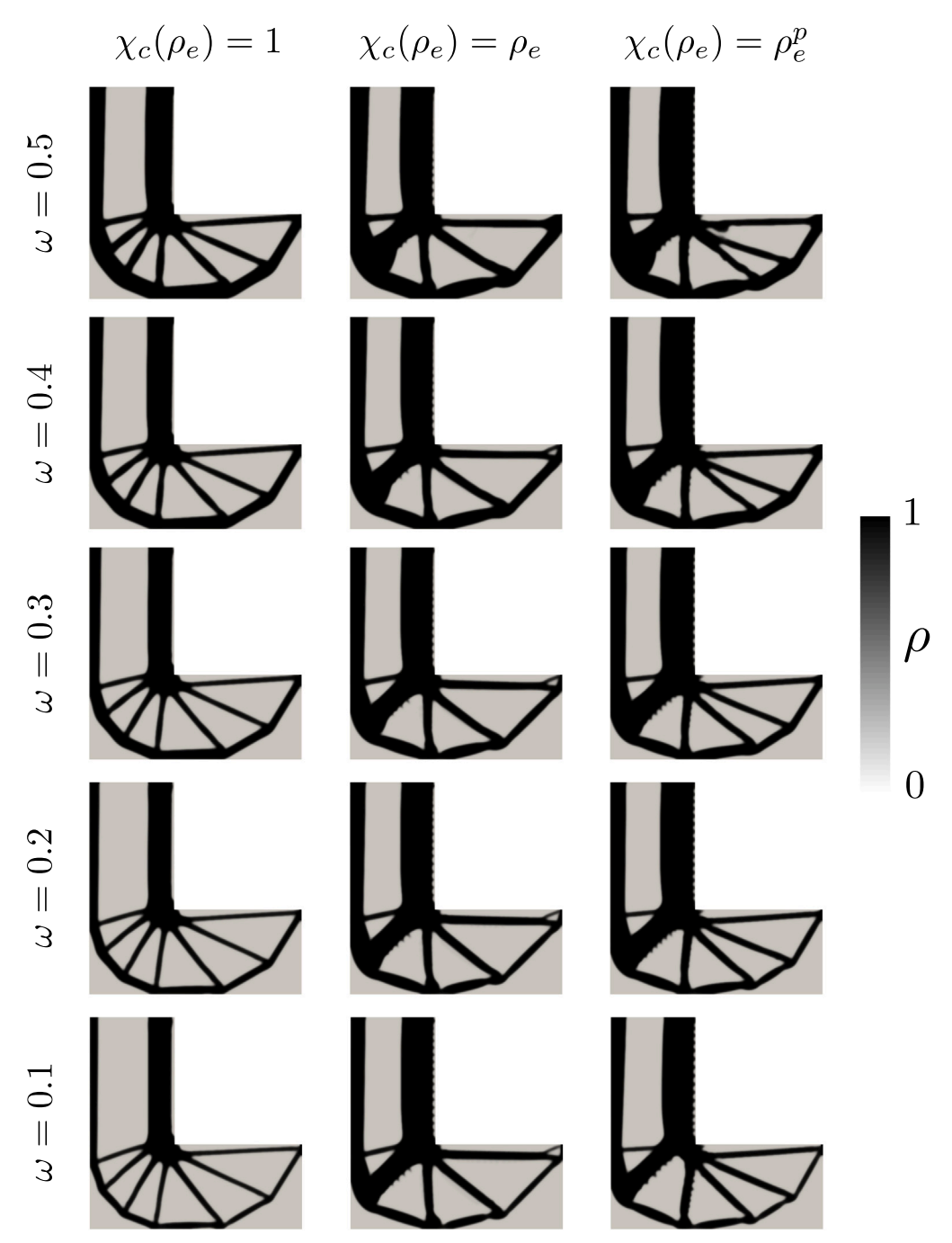


Fig. 25. Optimized topologies corresponding to different interpolations of the parameter c, the smallest L-bracket domain size considered (i.e., L=50 mm), double the original filter radius (i.e., $r_{\min}=2$ mm), and $\bar{\epsilon}_{\max}=\kappa_0$.

$$\frac{\partial h_{e_q}}{\partial \rho_e} = \begin{cases} \left(\frac{N_{\bar{e}}\bar{\underline{e}}}{\bar{\epsilon}_{\max}} - 1\right)^2 & \text{, if } N_{\bar{e}}\bar{\underline{e}} > \bar{\epsilon}_{\max} \\ 0 & \text{, otherwise} \end{cases} \qquad \frac{\partial h_{e_q}}{\partial \bar{\underline{e}}} = \begin{cases} \frac{2\rho_e}{\bar{\epsilon}_{\max}} & \left(\frac{N_{\bar{e}}\bar{\underline{e}}}{\bar{\epsilon}_{\max}} - 1\right)N_{\bar{e}} & \text{, if } N_{\bar{e}}\bar{\underline{e}} > \bar{\epsilon}_{\max} \\ \mathbf{0} & \text{, otherwise} \end{cases}$$

Recalling the assumption of plane stress and defining the constants, $c_1 \equiv (k-1)/(2k(1-2\nu))$, $c_2 \equiv 1/(2k)$, $c_3 \equiv (k-1)/(1-2\nu)$, $c_4 \equiv (12k)/((1+\nu)^2)$, $c_5 \equiv 2\left(1-\nu+\nu^2\right)$, $c_6 \equiv \left(4\nu-1-\nu^2\right)$ the final derivatives are provided below.

$$\frac{\partial \varepsilon_{eq}}{\partial I_1} = c_1 + \frac{c_2 c_3^2 I_1}{\sqrt{(c_3 I_1)^2 + c_4 J_2}} \qquad \qquad \frac{\partial \varepsilon_{eq}}{\partial J_2} = \frac{c_2 c_4}{2\sqrt{(c_3 I_1)^2 + c_4 J_2}}$$

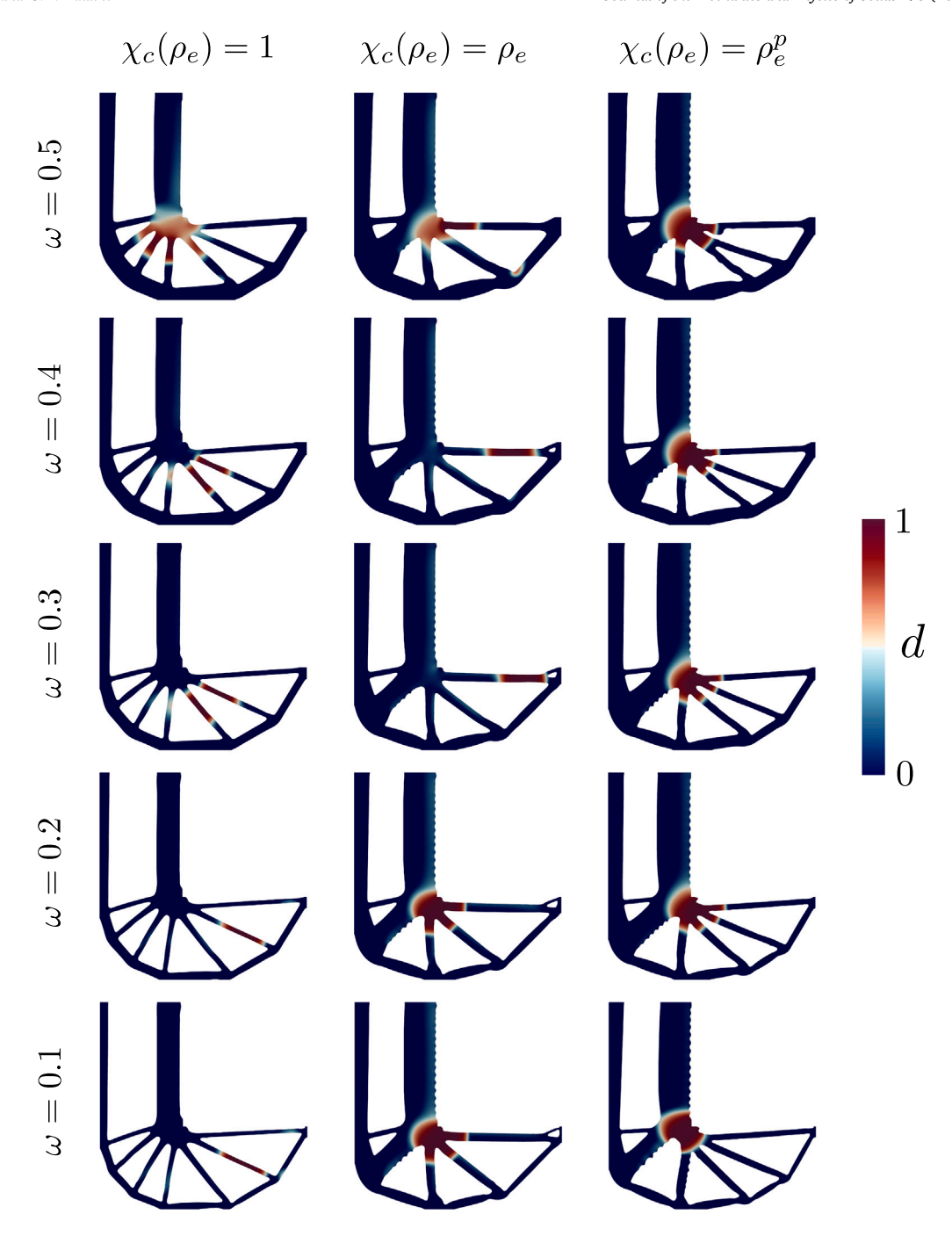


Fig. 26. Post-optimization verification simulation damage fields corresponding to the optimized topologies shown in Fig. 25.

$$\begin{split} \frac{\partial I_1}{\partial \varepsilon_{11}} &= \frac{2\nu - 1}{\nu - 1} & \frac{\partial I_1}{\partial \varepsilon_{22}} &= \frac{2\nu - 1}{\nu - 1} & \frac{\partial I_1}{\partial \varepsilon_{12}} &= 0 \\ \frac{\partial J_2}{\partial \varepsilon_{11}} &= \frac{c_5 \ \varepsilon_{11} + c_6 \ \varepsilon_{22}}{3(\nu - 1)^2} & \frac{\partial J_2}{\partial \varepsilon_{22}} &= \frac{c_5 \ \varepsilon_{22} + c_6 \ \varepsilon_{11}}{3(\nu - 1)^2} & \frac{\partial J_2}{\partial \varepsilon_{12}} &= 2\varepsilon_{12} \end{split}$$

To verify the analytical calculation for the AL function, we employ the portal frame geometry shown in Fig. 2 with L = 100. A coarse, unstructured finite element grid is used along with a non-uniform density field, both of which are illustrated in Fig. 27(a). The mesh consists of 663 quadrilateral elements and 718 nodes. A downward force of 50 N is applied over 3 element edges and identical numerical parameters corresponding to those provided in Table 2 are used, with the exception of c which is set to $8mm^2$

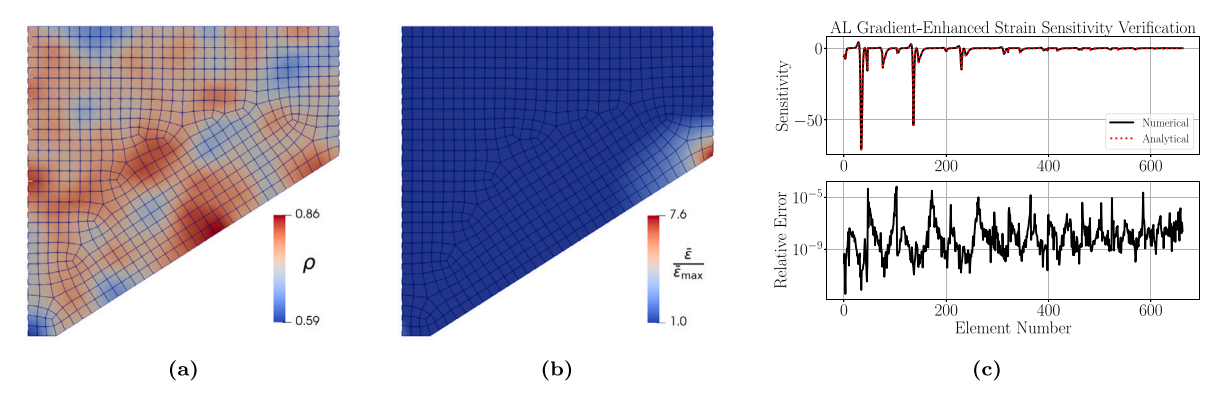


Fig. 27. Sensitivity verification problem with an unstructured mesh and random initial density field shown in (a). The ratio of the gradient-enhanced strain to its upper bound is shown in (b), and a numerical comparison of the sensitivity results are provided in (c).

and the filter radius $r_{\min} = 10$ mm due to the coarse finite element mesh. A penalty exponent of p = 2 is used, β_H is set to 1.5, and the initial Lagrange multiplier estimators are fixed to $\hat{\lambda}_{e_q}^{(1)} = 10$ globally. The ratio of gradient-enhanced strain to its upper bound (i.e., $\bar{\epsilon}_{\max} = \kappa_0$) when subject to the applied load is illustrated in Fig. 27(b). For each of the 663 design variables, an $O(\Delta z^4)$ finite difference approximation of the AL sensitivity is computed via,

$$\frac{df}{dz_e} \approx \frac{f(z_e - 2\Delta z) - 8f(z_e - \Delta z) + 8f(z_e + \Delta z) - f(z_e + 2\Delta z)}{12\Delta z} \tag{F.1}$$

where $\Delta z = 10^{-4}$ is the finite difference perturbation. Four perturbations are required for each of the 663 design variables, resulting in 2,652 forward analyses required in order to compute the full numerical approximation of the relevant gradient. This is compared against the analytical calculation for which the results are illustrated in Fig. 27(c) along with the corresponding relative error.

Appendix G. Nomenclature

 E_0 Young's modulus of solid material

 N_{elem} Number of finite elements

 N_{auad} Number of quadrature points per finite element

 \hat{k} AL iteration number

 \mathbb{C}_0 Solid material constitutive tensor

 $c = \ell_{\bar{\epsilon}}^2$ Gradient-enhanced strain length scale parameter

d Damage variable

 g_{e_a} Element e, quadrature point q local constraint

 $h_{e_{-}}$ Modified local constraint of element e, quadrature point, q

k Compressive-to-tensile strength ratio

p SIMP penalization parameter

 r_{\min} Filter radius

α Damage evolution equation parameter

 β Damage evolution equation parameter

 β_H Aggressiveness parameter used in the projection function

 χ_E Elastic modulus interpolation function

 χ_c Length scale parameter interpolation function

 $\chi_{\varepsilon_{aa}}$ Equivalent strain interpolation function

 ϵ Ersatz stiffness parameter

 η Damage evolution artificial viscosity parameter

 η_H Threshold parameter used in the projection function

 $\bar{\varepsilon}$ Gradient-enhanced equivalent strain

 $\bar{\varepsilon}_{\max}$ Gradient-enhanced equivalent strain limit

 $\hat{\alpha}$ Parameter used to update the penalty factors, $\hat{\mu}_{e}^{(\hat{k})}$

 $\hat{\lambda}_{e_{-}}^{(\hat{k})}$ Element e, quadrature point q Lagrange estimator for the \hat{k} -th AL subproblem

 $\hat{\mu}_{max}$ Maximum penalty factor

 $\hat{\mu}_{e_a}^{(k)}$ Element e, quadrature point q penalty factor for the \hat{k} -th AL subproblem

- $\hat{\rho}$ Filtered design variables
- κ_0 Initial threshold for damage evolution
- ν Poisson's ratio
- ω Weighting parameter in aggregate objective function
- ρ_a Pseudo-density of element e
- ε_{eq} Equivalent strain measure
- $R_{\bar{e}}$ Gradient-enhanced equivalent strain residual vector
- R_u Linear momentum residual vector
- V Vector of element volumes/areas
- $\bar{\epsilon}$ Vector of nodal gradient-enhanced strains
- u Vector of nodal displacements
- f_{ext} External force vector
 - t Applied traction vector
 - z Vector of design variables
 - λ Linear momentum adjoint vector
 - μ Gradient-enhanced strain adjoint vector
 - σ Cauchy stress tensor
 - ε Small strain tensor

References

Amestoy, P.R., Duff, I.S., Koster, J., L'Excellent, J.-Y., 2001. A fully asynchronous multifrontal solver using distributed dynamic scheduling. SIAM J. Matrix Anal. Appl. 23 (1), 15–41.

Amir, O., 2013. A topology optimization procedure for reinforced concrete structures. Comput. Struct. 114-115, 46-58.

Amir, O., Sigmund, O., 2013. Reinforcement layout design for concrete structures based on continuum damage and truss topology optimization. Struct. Multidiscip. Optim. 47 (2), 157–174.

Arndt, D., Bangerth, W., Blais, B., Fehling, M., Gassmöller, R., Heister, T., Heltai, L., Köcher, U., Kronbichler, M., Maier, M., Munch, P., Pelteret, J.-P., Proell, S., Simon, K., Turcksin, B., Wells, D., Zhang, J., 2021. The deal.II library, Version 9.3. J. Numer. Math. 29 (3), 171–186.

Baier, H., 1994. Ill-posed problems in structural optimization and their practical consequences. Struct. Optim. 7 (3), 184-190.

Balay, S., Abhyankar, S., Adams, M.F., Brown, J., Brune, P., Buschelman, K., Dalcin, L., Eijkhout, V., Gropp, W.D., Kaushik, D., Knepley, M.G., May, D.A., McInnes, L.C., Mills, R.T., Munson, T., Rupp, K., Sanan, P., Smith, B.F., Zampini, S., Zhang, H., Zhang, H., 2018. PETSc Users Manual. Technical Report, (ANL-95/11 - Revision 3.9), Argonne National Laboratory.

Barbier, T., Shakour, E., Sigmund, O., Lombaert, G., Schevenels, M., 2022. Topology optimization of damage-resistant structures with a predefined load-bearing capacity. Internat. J. Numer. Methods Engrg. 123 (4), 1114–1145.

Bažant, Z.P., 2004. Scaling theory for quasibrittle structural failure. Proc. Natl. Acad. Sci. 101 (37), 13400-13407.

Bažant, Z.P., Belytschko, T.B., Chang, T.-P., 1984. Continuum theory for strain-softening. J. Eng. Mech. 110 (12), 1666-1692.

Bažant, Z.P., Jirásek, M., 2002. Nonlocal integral formulations of plasticity and damage: Survey of progress. J. Eng. Mech. 128 (11), 1119-1149.

Bendsøe, M.P., 1989. Optimal shape design as a material distribution problem. Struct. Optim. 1 (4), 193-202.

Bendsøe, M.P., Kikuchi, N., 1988. Generating optimal topologies in structural design using a homogenization method. Comput. Methods Appl. Mech. Engrg. 71 (2), 197–224.

Bertsekas, D.P., 1999. Nonlinear Programming, second ed. Athena Scientific.

Bruggi, M., 2008. On an alternative approach to stress constraints relaxation in topology optimization. Struct. Multidiscip. Optim. 36 (2), 125-141.

Engelen, R.A.B., Geers, M.G.D., Baaijens, F.P.T., 2003. Nonlocal implicit gradient-enhanced elasto-plasticity for the modelling of softening behaviour. Int. J. Plast. 19 (4), 403–433.

Gao, H., Huang, Y., Nix, W.D., Hutchinson, J.W., 1999. Mechanism-based strain gradient plasticity—I. Theory. J. Mech. Phys. Solids 47 (6), 1239–1263.

Giraldo-Londono, O., Paulino, G.H., 2020. A unified approach for topology optimization with local stress constraints considering various failure criteria: von Mises, Drucker-Prager, Tresca, Mohr-Coulomb, Bresler- Pister and Willam-Warnke. Proc. R. Soc. A 476 (2238), 20190861.

Giraldo-Londoño, O., Russ, J.B., Aguiló, M.A., Paulino, G.H., 2022. Limiting the first principal stress in topology optimization: a local and consistent approach. Struct. Multidiscip. Optim. 65 (9), 254.

Hillerborg, A., Modéer, M., Petersson, P.E., 1976. Analysis of crack formation and crack growth in concrete by means of fracture mechanics and finite elements. Cem. Concr. Res. 6 (6), 773–781.

James, K.A., Waisman, H., 2014. Failure mitigation in optimal topology design using a coupled nonlinear continuum damage model. Comput. Methods Appl. Mech. Engrg. 268 (Supplement C), 614–631.

Lazarov, B.S., Sigmund, O., 2011. Filters in topology optimization based on Helmholtz-type differential equations. Internat. J. Numer. Methods Engrg. 86 (6), 765–781.

Li, L., Khandelwal, K., 2017. Design of fracture resistant energy absorbing structures using elastoplastic topology optimization. Struct. Multidiscip. Optim. 1–29. Li, L., Zhang, G., Khandelwal, K., 2018. Failure resistant topology optimization of structures using nonlocal elastoplastic-damage model. Struct. Multidiscip. Optim. 1–30.

Mazars, J., Pijaudier-Cabot, G., 1989. Continuum damage theory—Application to concrete. J. Eng. Mech. 115 (2), 345-365.

Miehe, C., Schänzel, L.-M., Ulmer, H., 2015. Phase field modeling of fracture in multi-physics problems. Part I. Balance of crack surface and failure criteria for brittle crack propagation in thermo-elastic solids. Comput. Methods Appl. Mech. Engrg. 294, 449–485.

Miehe, C., Welschinger, F., Hofacker, M., 2010. Thermodynamically consistent phase-field models of fracture: Variational principles and multi-field FE implementations. Internat. J. Numer. Methods Engrg. 83 (10), 1273–1311.

Nguyen, H., Pathirage, M., Rezaei, M., Issa, M., Cusatis, G., Bažant, Z.P., 2020. New perspective of fracture mechanics inspired by gap test with crack-parallel compression. Proc. Natl. Acad. Sci. 117 (25), 14015–14020.

Nocedal, J., Wright, S., 2006. Numerical Optimization, second ed. In: Springer Series in Operations Research and Financial Engineering, Springer-Verlag, New York.

Peerlings, R.H.J., de Borst, R., Brekelmans, W.a.M., Geers, M.G.D., 1998. Gradient-enhanced damage modelling of concrete fracture. Mech. Cohes.-Frict. Mater 3 (4), 323–342.

- Peerlings, R.H.J., De Borst, R., Brekelmans, W.a.M., De Vree, J.H.P., 1996. Gradient enhanced damage for quasi-brittle materials. Internat. J. Numer. Methods Engrg. 39 (19), 3391–3403.
- Pijaudier-Cabot, G., Bažant, Z.P., 1987. Nonlocal damage theory. J. Eng. Mech. 113 (10), 1512-1533.
- Russ, J.B., Waisman, H., 2020a. A novel elastoplastic topology optimization for enhanced failure resistance via local ductile failure constraints and linear buckling analysis. Comput. Methods Appl. Mech. Engrg. 373, 113478.
- Russ, J.B., Waisman, H., 2020b. A novel topology optimization formulation for enhancing fracture resistance with a single quasi-brittle material. Internat. J. Numer. Methods Engrg. 121 (13), 2827–2856.
- Senhora, F.V., Giraldo-Londoño, O., Menezes, I.F.M., Paulino, G.H., 2020. Topology optimization with local stress constraints: a stress aggregation-free approach. Struct. Multidiscip. Optim. 62 (4), 1639–1668.
- Sigmund, O., Petersson, J., 1998. Numerical instabilities in topology optimization: A survey on procedures dealing with checkerboards, mesh-dependencies and local minima. Struct. Optim. 16 (1), 68–75.
- da Silva, G.A., Aage, N., Beck, A.T., Sigmund, O., 2021. Three-dimensional manufacturing tolerant topology optimization with hundreds of millions of local stress constraints. Internat. J. Numer. Methods Engrg. 122 (2), 548–578.
- Simo, J.C., Ju, J.W., 1987. Strain- and stress-based continuum damage models-I. Formulation. Int. J. Solids Struct. 23 (7), 821-840.
- Svanberg, K., 1987. The method of moving asymptotes—a new method for structural optimization. Internat. J. Numer. Methods Engrg. 24 (2), 359-373.
- Svanberg, K., 2007. MMA and GCMMA two methods for nonlinear optimization. Technical report, p. 15.
- de Vree, J.H.P., Brekelmans, W.A.M., van Gils, M.A.J., 1995. Comparison of nonlocal approaches in continuum damage mechanics. Comput. Struct. 55 (4), 581–588.
- Wächter, A., Biegler, L.T., 2006. On the implementation of an interior-point filter line-search algorithm for large-scale nonlinear programming. Math. Program. 106 (1), 25–57.
- Wallin, M., Ivarsson, N., Amir, O., Tortorelli, D., 2020. Consistent boundary conditions for PDE filter regularization in topology optimization. Struct. Multidiscip. Optim. 62 (3), 1299–1311.
- Wang, F., Lazarov, B.S., Sigmund, O., 2011. On projection methods, convergence and robust formulations in topology optimization. Struct. Multidiscip. Optim. 43 (6), 767–784.
- Xia, L., Da, D., Yvonnet, J., 2018. Topology optimization for maximizing the fracture resistance of quasi-brittle composites. Comput. Methods Appl. Mech. Engrg. 332, 234-254.
- Zhou, M., Rozvany, G.I.N., 1991. The COC algorithm, Part II: Topological, geometrical and generalized shape optimization. Comput. Methods Appl. Mech. Engrg. 89 (1), 309–336.